



HAL
open science

Seismic properties of mantle metasomatism from mantle xenoliths beneath the North Tanzania Divergence, East African Rift

Adeline Clutier, Fleurice Parat, Benoît Gibert, Michel Grégoire, Christel Tiberi, Stéphanie Gautier

► To cite this version:

Adeline Clutier, Fleurice Parat, Benoît Gibert, Michel Grégoire, Christel Tiberi, et al.. Seismic properties of mantle metasomatism from mantle xenoliths beneath the North Tanzania Divergence, East African Rift. *Gondwana Research*, 2024, 131, pp.278-299. 10.1016/j.gr.2024.03.008 . hal-04652492

HAL Id: hal-04652492

<https://hal.science/hal-04652492>

Submitted on 18 Jul 2024

HAL is a multi-disciplinary open access archive for the deposit and dissemination of scientific research documents, whether they are published or not. The documents may come from teaching and research institutions in France or abroad, or from public or private research centers.

L'archive ouverte pluridisciplinaire **HAL**, est destinée au dépôt et à la diffusion de documents scientifiques de niveau recherche, publiés ou non, émanant des établissements d'enseignement et de recherche français ou étrangers, des laboratoires publics ou privés.

Journal Pre-proofs

Seismic properties of mantle metasomatism from mantle xenoliths beneath the North Tanzania Divergence, East African Rift

A. Clutier, F. Parat, B. Gibert, M. Grégoire, C. Tiberi, S. Gautier

PII: S1342-937X(24)00066-2
DOI: <https://doi.org/10.1016/j.gr.2024.03.008>
Reference: GR 3239

To appear in: *Gondwana Research*

Received Date: 7 March 2023
Revised Date: 23 February 2024
Accepted Date: 3 March 2024

Please cite this article as: A. Clutier, F. Parat, B. Gibert, M. Grégoire, C. Tiberi, S. Gautier, Seismic properties of mantle metasomatism from mantle xenoliths beneath the North Tanzania Divergence, East African Rift, *Gondwana Research* (2024), doi: <https://doi.org/10.1016/j.gr.2024.03.008>

This is a PDF file of an article that has undergone enhancements after acceptance, such as the addition of a cover page and metadata, and formatting for readability, but it is not yet the definitive version of record. This version will undergo additional copyediting, typesetting and review before it is published in its final form, but we are providing this version to give early visibility of the article. Please note that, during the production process, errors may be discovered which could affect the content, and all legal disclaimers that apply to the journal pertain.

© 2024 International Association for Gondwana Research. Published by Elsevier B.V. All rights reserved.



Title: Seismic properties of mantle metasomatism from mantle xenoliths beneath the North Tanzania Divergence, East African Rift

Authors: Clutier¹, A., Parat¹, F., Gibert¹, B., Grégoire², M., Tiberi¹, C., Gautier¹, S.

Affiliation: ¹ Géosciences Montpellier, Université de Montpellier, CNRS, CC060, Place Eugène Bataillon, 34095 Montpellier Cedex 05, France

² Géosciences Environnement Toulouse (GET), Université de Toulouse, UMR 5563 CNRS/UPS/IRD/CNES, 14 Avenue Edouard Belin, 31400 Toulouse, France

Contact: adeline.clutier@umontpellier.fr

Key words: mantle xenolith, seismic properties, alkaline magma, mantle metasomatism, rift initiation, East African Rift

Highlights:

- Mantle at rift initiation is metasomatized by alkaline fluids at 40-90 km depth
- 1100°C mantle isotherm relates to the volatile-bearing peridotite solidus
- Lithospheric mantle has ≈20% of crystallized or ≈10% of fluid-filled vertical veins

1 Abstract

2 We use mantle xenoliths brought to the surface by alkaline lavas to determine the
3 chemical and physical properties of the metasomatized lithospheric mantle that contribute to
4 the earliest rifting stage in East Africa. Our results help to interpret the seismic tomographic
5 images in terms of vein and inclusions proportions in the lithospheric mantle. We focus on
6 mantle xenoliths from the in-rift Pello Hill volcano in the North Tanzanian Divergence (NTD).
7 These xenoliths reveal the presence of refractory mantle harzburgites and dunites with coarse
8 granular to porphyroclastic textures and 6 to 80% of diopside, phlogopite and amphibole-
9 bearing veins and phlogopite-rich hornblendite xenolith. The presence of calc-potassic and
10 FeO, TiO₂-rich veins, and mineral equilibria of olivine and pyroxenes indicate that fluid/melt-
11 rock interactions occurred at depth from 40 km to 80-90 km, and indicate the presence of a
12 high-temperature isotherm beneath the NTD (T=1040-1200°C). We computed the seismic
13 properties of the mantle xenoliths with different proportions, compositions, and geometric
14 distributions of crystallized and fluid-filled veins. Compared to vein-free peridotites, for
15 crystallized vein-bearing xenoliths, the velocity is lowered by 2-4% to 28-37% for V_p and by 2-
16 3% to 25-29% for V_s for 6% to 60% veins, respectively. For fluid-filled inclusions, hydrous melt
17 lens-shape inclusions are the most effective parameter to reduce P velocity, compared to dry
18 or 2.5%-CO₂ peridotitic melt. A comparison with seismic tomography velocities allows us to
19 discuss the current state of the lithospheric mantle. The best agreement obtained between P
20 teleseismic tomography (V_p anomalies between -9% and -15%) and vein-bearing peridotites
21 (depth 40-90 km) corresponds to 12-25% of crystallized veins or 8-15% for fluid filled-veins for
22 a vertical foliation and transtensional strain regime in the mantle lithosphere beneath the
23 NTD.

24

25 1 Introduction

26 A remaining challenge for the geophysics and rock physics communities is to separate
27 the different factors affecting seismic properties such as pressure, temperature,
28 compositional variations, fluid presence or mantle anisotropy (Almqvist and Mainprice, 2017;
29 Deschamps and Trampert, 2003; Mavko et al., 2020). Partial melt signature is particularly
30 problematic as different factors may produce similar decreasing effects on seismic velocities
31 (temperature increase, change of shape or increase of size of melt pockets, fluid presence,
32 anisotropy...) (Almqvist and Mainprice, 2017; Deschamps and Trampert, 2003; Mainprice,
33 1997). Laboratory experiments and models have been extensively carried out to quantify
34 these melt effects on seismic velocities and have pointed out a non-linear relationship with a
35 strong dependency on the shape and orientation of the melt pocket (Clark and Leshner, 2017;
36 Goes et al., 2000; Hammond and Kendall, 2016). Seismic velocity also relates to intrinsic
37 properties of rocks (from minerals) and extrinsic components (open cracks, crystallized and
38 fluid-filled veins, alteration) (Almqvist and Mainprice, 2017). Mantle metasomatism is one
39 cause for a change in the seismic properties of the rocks, as it affects both their intrinsic and
40 extrinsic components (Dawson, 1984; O'Reilly and Griffin, 2013). The percolation of
41 anhydrous, hydrous, or carbonatitic silicate melts overprints the mantle lithosphere signature.
42 It modifies the viscoelastic and chemical properties by forming compositionally distinct
43 secondary phases (interstitial minerals, metasomatic veins) or by modifying minerals
44 equilibrium (modal and cryptic metasomatism, respectively, Dawson, 1984; O'Reilly and

45 Griffin, 2013). The presence of new metasomatic minerals, such as amphibole or phlogopite,
46 may in turn, affect the seismic properties of the metasomatized mantle. When metasomatism
47 is related to a mantle plume, it also alters the geotherm and, consequently, the seismic
48 velocities observed in tomographic models (e.g., Allen et al., 2002; Grijalva et al., 2018).

49 In this study, we aim to quantify the effect of metasomatism on lithospheric seismic
50 velocities. We take advantage of xenoliths collected in the East African rift, in the so-called
51 North Tanzanian Divergence (NTD). Here, the Archaean sub-continental lithospheric mantle
52 has experienced multiple metasomatic events that have modified its composition and
53 rheology (Dawson, 1997; Koornneef et al., 2009; Lee and Rudnick, 1999). In particular, the
54 most recent impingement of the East Africa mantle plume has modified the geotherm and
55 also carried an interaction of volatile-rich melts or fluids with peridotitic mantle (Baptiste et
56 al., 2015; Gibson et al., 2013; Mulibo and Nyblade, 2013a; Reiss et al., 2021; Selway et al.,
57 2014). In order to evaluate the role of the metasomatic agent on the lithospheric mantle, we
58 perform petrological and petrophysical investigations for vein-bearing, and vein-free mantle
59 xenoliths from Pello Hill in the NTD to: (1) characterize the chemistry, and the depth of the
60 melt/fluid percolation within the lithospheric mantle; (2) determine the seismic properties of
61 the metasomatized mantle; and (3) estimate the proportion of fluid circulating within the
62 lithospheric mantle by comparing seismic properties of mantle xenoliths and P-wave
63 tomographic images. In this study, we evaluate the link between geophysical and petrological
64 data based on: (1) observations made on natural samples considered representative for the
65 lithospheric mantle beneath the NTD; and (2) constraints from modeling based on
66 experimental mineral and rock physics laboratory measurements.

67

68 **2 The North Tanzanian Divergence**

69 The North Tanzanian Divergence is located at the southern tip of the Eastern branch
70 of the East African Rift. This zone is a relatively young continental rifting zone (~8 Ma, Le Gall
71 et al., 2008), compared to the Afar mature zone (45-35 Ma, e.g., Courtillot et al., 1999;
72 Courtillot and Renne, 2003; Ebinger and Sleep, 1998; George et al., 1998) and represents the
73 initial stages of the rifting process. In the NTD, the complex interaction between inherited
74 structures in the highly heterogeneous lithosphere and deep mantle processes leads to diffuse
75 tectonic deformation and magmatism at the surface (Huerta et al., 2009; MacDonald et al.,
76 2001; Mulibo and Nyblade, 2013b; O'Donnell et al., 2013; Pik et al., 2006; Tiberi et al., 2019;
77 Weeraratne et al., 2003). The narrow, poorly magmatic Kenya rift abruptly widens when
78 reaching North Tanzania (~3° S) and splits into three different arms: the Eyasi, Manyara and
79 Pangani branches (Figure 1, Corti et al., 2013; Le Gall et al., 2008). These branches develop
80 mainly in Proterozoic mobile belts, at the edge of (or in) cratonic units (Tanzanian Craton and
81 Masai block) with magmatism occurring since ~8-5 Ma (Dawson, 1992; Mana et al., 2015), and
82 a tectonic expression since ~3 Ma (Foster et al., 1997). The volcanism preceded the faulting
83 by ~20 Ma in the Afar (Ebinger et al., 2000), and by a few Ma in the Kenyan rift and in the NTD
84 (Le Gall et al., 2008; Mechie et al., 1997).

85 The North Tanzania Divergence volcanism is related to the presence of a mantle
86 plume (Adams et al., 2012; MacDonald et al., 2001; Nyblade et al., 2000). The NTD displays
87 broadly distributed volcanic edifices with a highly heterogeneous chemical signature (Dawson,

88 2008; Mana et al., 2015). It encompasses the oldest pre-rift volcano Essimingor and the only
89 active carbonatitic edifice, Oldoinyo Lengai. On a N-S axis, in-rift volcanism is highly alkaline
90 (e.g., Baudouin et al., 2016; Baudouin and Parat, 2020; Klaudius and Keller, 2006; Lee and
91 Rudnick, 1999) and sub-alkaline to alkaline for the E-W axis (Braunger et al., 2021; Mana et
92 al., 2015, 2012; Mollel et al., 2008; Nonnotte, 2007; Roberts, 2003; Wilkinson et al., 1986)
93 (Figure 1). This diversity of magmas results from variable amount (3-6% to 1%, Baudouin and
94 Parat, 2020; Mana et al., 2015) and depths of partial melting. From north to south of the NTD
95 the depth of partial melting increases, from 75-90 km in the Natron-Engaruka basins
96 (Mattsson et al., 2013), and up to 110-130 km for Kwahara and 150 km for Labait volcanoes
97 (Baudouin and Parat, 2020; Gibson et al., 2013).

98 Although the magmatism strongly highlights the presence of recent mantle
99 metasomatism by alkaline melts, previous Re/Os and Nd/Sm isotope studies indicate the
100 presence of ancient events, during the Precambrian or Pan African orogens (Burton et al.,
101 2000; Chesley et al., 1999; Koornneef et al., 2009). The records of recent and ancient
102 metasomatic equilibrium indicate that the lithospheric mantle below the NTD is highly
103 heterogeneous and that long-term metasomatism is still present. In the NTD, five volcanoes
104 erupted mantle xenoliths: Eledoi, Pello Hill, Lashaine, Olmani, and Labait (Figure 1). Combined
105 with information from the magmatism, these xenoliths give an insight of the past and almost-
106 current mantle state at depth, and allow an estimate of the impact of metasomatism on
107 seismic properties.

108

109 **2.1 Lithospheric mantle metasomatism beneath the NTD**

110 At the NTD, the strong and thick (150-180 km) cratonic lithosphere of the Tanzanian
111 craton highly contrasts with the thinner and younger Proterozoic mobile belt lithosphere
112 (Figure 1, Craig et al., 2011; Fishwick, 2010; Lee and Rudnick, 1999; Tiberi et al., 2019). The
113 roughly N-S suture between these units is thought to have played a first-order structural
114 control on the evolution of the rift (Corti et al., 2013; Ebinger et al., 1997; Koptev et al., 2018,
115 2015). Pre-existing zones of weakness could have prevented the cratonic lithosphere from
116 being deformed by accommodating external stresses (Lenardic et al., 2003). It may also have
117 channelized the mantle upwelling and generation of melts and/or deep fluid-rock interactions
118 inducing modal and/or cryptic metasomatism (Albaric et al., 2009; Baker et al., 1998; Delpech
119 et al., 2004; Dixon et al., 2008; Grégoire et al., 2000; Koptev et al., 2016; O'Reilly and Griffin,
120 1988; Wölbern et al., 2012).

121

122 **2.1.1 Cratonic mantle**

123 The Tanzania cratonic lithospheric mantle, down to ~120 km, has a mean Re-Os age
124 of 2.8-2.0 Ga (xenoliths from the on-craton border Labait volcano, Chesley et al., 1999),
125 suggesting that refractory lithospheric mantle has been metasomatized during a 2.8 Ga melt
126 event. Nd ages of 2.1-1.76 Ga, associated with a Light Rare Earth Elements enrichment in
127 clinopyroxenes from spinel or garnet-bearing peridotites, may indicate cryptic metasomatism
128 induced by subduction-related fluid/melt during the Usagaran belt formation (Koornneef et

129 al., 2009). Deeper garnet-bearing xenoliths (> 120 km) have Re-Os model ages < 1 Ga and are
130 younger than the spinel-bearing xenoliths, suggesting a more recent melting event that
131 overprinted the 2.8 Ga event (Chesley et al., 1999). This is also confirmed by Nd model ages
132 of 698-639 Ma, associated with hydrous fluids, possibly coming from subduction related to
133 the Pan-African Orogeny and/or to the plume ascension and rift opening (Hui et al., 2015;
134 Koornneef et al., 2009). The north Tanzania lithospheric mantle is therefore heterogeneous,
135 with at least two metasomatic events, resulting from asthenospheric Fe-rich melts (Lee and
136 Rudnick, 1999) and silicic fluid circulation (Aulbach et al., 2011). The mantle below Labait has
137 an isotropic composition intermediate between the Depleted Mantle (DM) and Enriched
138 Mantle 1 (EM1) reservoirs that has been associated with former subduction (Aulbach et al.,
139 2011). The occurrence of deep metasomatic processes is also supported by the microstructure
140 of xenoliths, where neoblasts crystallized (due to temperature increase) in the deepest
141 garnet-free and uppermost garnet-bearing xenoliths (Vauchez et al., 2005).

142

143 **2.1.2 In-rift mantle**

144 Below the Masai block and the East-West volcanic axis (in-rift xenoliths from Lashaine
145 and Olmani volcanoes), the lithospheric mantle is at least 3.4 Ga old (Burton et al., 2000) and
146 was also subject to different metasomatic events. A melting event was dated by U-Pb for
147 Lashaine garnet-bearing xenoliths at 2.0 Ga, and Re-Os analyses on silicate minerals from
148 garnet-bearing Lashaine xenoliths display ages of 15.4-31.4 Ma (Burton et al., 2000; Cohen et
149 al., 1984). The garnet-bearing peridotites have higher Al₂O₃, CaO and Na₂O concentrations
150 than garnet-free peridotites, but both have similar Mg# (Gibson et al., 2013; Rudnick et al.,
151 1994). These compositions were interpreted reflecting fluid/melt derived from subducted
152 oceanic crust, and the EM1 and EM2 reservoirs as detrital sediment component in the hotter
153 Archean mantle (Aulbach et al., 2011; Rudnick et al., 1994). The metasomatism in Olmani
154 xenoliths is marked by the presence of clinopyroxene and phosphates, suggesting an
155 interaction of the peridotites with carbonatitic melt (Rudnick et al., 1994).

156 Below the Pello Hill volcano, the lithosphere was dated to at least 1.3 Ga by Re-Os isotopes
157 for a lherzolite, and Os model ages might indicate an Archean lithosphere (Aulbach et al.,
158 2011). A negative correlation of Re-Os isotopes evolution may suggest that the lithospheric
159 mantle has been metasomatized less than 16 Ma ago by melts with silicic and carbonatitic
160 intermediate compositions (Aulbach et al., 2011; Burton et al., 2000). In addition, isotopic
161 signatures for Ol Doinyo Lengai and the Ngorongoro volcanic complex are evidence of even
162 more diverse enriched mantle signatures (HIMU and EM1, Aulbach et al., 2011; Bell and
163 Simonetti, 1996; Mollet et al., 2011, 2009).

164

165 **3 Methods**

166 **3.1 Samples**

167 To overview the lithospheric mantle metasomatism below the in-rift Pello Hill
168 volcano, we selected a representative set of 12 xenoliths with and without veins, and with

169 variable amounts of interstitial metasomatic minerals Table 1. Among those 12 samples, 7
170 samples are free of veins (PH1, PH2, PH8, PH13, PH17, PH24, PH26) and 4 samples have 6 to
171 80% of clinopyroxene-phlogopite-amphibole veins crosscutting the xenoliths (PH4, PH9, PH18
172 and PH27). The host xenoliths are dunites (PH4, PH8, PH9, PH18 and PH26) and harzburgites
173 (PH1, PH2, PH13, PH17, PH24 and PH27), plus 1 phlogopite-rich, olivine-, and clinopyroxene-
174 bearing hornblendite (PH23). We made 12 thin sections, perpendicular to the veins if present,
175 in order to have a representative vein proportion of the mantle xenoliths and to perform
176 EPMA and EBSD analyses.

177

178 3.2 Pressure and temperature estimate

179 Major element concentrations of minerals were measured at the Paul Sabatier
180 University of Toulouse, with a Cameca SXFive electron microprobe (EPMA). The analyses were
181 carried out with an accelerating voltage of 15 kV, a 10 or 20 nA beam current depending on
182 the mineral resistance under the beam (10 nA for amphibole and phlogopite; 20 nA for olivine,
183 pyroxene, garnet, and oxides), a focused beam (inferior to the μm) for olivine, clinopyroxene,
184 orthopyroxene, garnet, oxide and defocused (2 μm) for amphibole and phlogopite. The
185 analyzed surface is about $2 \times 2 \mu\text{m}^2$. The counting time was fixed to 10 seconds for all elements
186 except for fluorine which was set to 20 seconds. The standards used for calibration were albite
187 for Na, wollastonite for Si and Ca, Al_2O_3 for Al, sanidine for K, MnTiO_3 for Mn and Ti, Fe_2O_3 for
188 Fe, topaz for F, MgO for Mg, tugtupite for Cl, BaSO_4 for Ba, Cr_2O_3 for Cr, SrSO_4 -MAC for S,
189 native metal for Cu and Ni (Ni-G5), and sphalerite for Zn.

190 We estimate the equilibration depth and temperature of mantle xenoliths using
191 orthopyroxene-clinopyroxene and olivine-clinopyroxene equilibria that have been calibrated
192 experimentally by Brey and Köhler (1990) and Köhler and Brey (1990), respectively. The
193 equilibria between orthopyroxene-clinopyroxene and olivine-clinopyroxene were tested by
194 using Fe/Mg partitioning between minerals ($\text{Fe}^{2+}/\text{Mg} \times 100$, Brey and Köhler, 1990; Putirka,
195 2008, and Supplementary Material 1). For all mineral equilibrium, we chose grains as close as
196 possible to each other, and far from veins. By using the two-pyroxenes thermometer from
197 Putirka (2008), we determined an a priori equilibrium temperature (T_{input}). Then, an a priori
198 pressure (P_{input}) is determined graphically from the geotherm modified by a plume thermal
199 anomaly from Selway et al. (2014) and T_{input} . Finally, T_{input} and P_{input} were implemented in
200 PTEXL3 spreadsheet (from T. Koehler and modified by A. Girnis; [http://www.mineralogie.uni-](http://www.mineralogie.uni-frankfurt.de/index.html)
201 [frankfurt.de/index.html](http://www.mineralogie.uni-frankfurt.de/index.html)), where the final temperatures is determined with the
202 orthopyroxene-clinopyroxene equilibrium from Brey and Köhler (1990). In the case of
203 xenoliths without orthopyroxene, the partitioning of Ca between the olivine and the
204 clinopyroxene from Köhler and Brey (1990) was used. The final pressure was computed using
205 Ca partitioning between the olivine and the clinopyroxene from Köhler and Brey (1990) for
206 the garnet-free mantle xenoliths from Pello Hill.

207 The calcium concentration in olivine was measured with EPMA, and several analyses
208 were confirmed by Laser Ablation Inductively Coupled Plasma Mass Spectrometry (LA-ICPMS)
209 at AETE-ISO platform (OSU OREME, University of Montpellier). A 130 μm diameter laser beam
210 was used for olivine with a pulsed 193 nm Excimer CompEx 102 laser (GeoLas Q+ platform).
211 The laser repetition rate was 6 Hz and the laser power was 5.75-6 $\text{J}\cdot\text{cm}^{-2}$. Concentrations were

212 calibrated with the intern standard NIST612, and SiO₂ concentrations were previously
 213 measured by the electron microprobe. The external standard is BIR. The raw laser data were
 214 processed with GLITTER software (Griffin et al., 2009), which converts the signal (signal
 215 intensity/time) to elemental concentrations. For thermobarometry, the pressure-
 216 temperature (P-T) conditions were computed using both microprobe and LA-ICPMS analyses.

217

218 **3.3 Crystallographic preferred orientation**

219 We analyzed ten samples with the Camscan Crystal Probe X500FE Electron Back
 220 Scattered Diffraction (EBSD) microscope at Geosciences Montpellier (MEA platform,
 221 University of Montpellier) to determine the crystallographic preferred orientation (CPO) and
 222 phase proportion of olivine, clinopyroxene, orthopyroxene, phlogopite, amphibole, and
 223 oxides. Measurements were performed using an acceleration voltage of 20 kV and an average
 224 working distance of 25 mm. For each sample, the map covers almost the entire thin section
 225 (30×40 mm). The step size between hitting points varies from 12 to 40 μm depending on the
 226 sample. The indexing rate varies between 84% (PH23, olivine-clinopyroxene-phlogopite-
 227 amphibole-oxide vein) and 96% (PH26 dunite), depending on the mineral species and the
 228 degree of fractures in the sample. The lowest indexing rates are for samples containing a high
 229 proportion of phlogopite, which is difficult to index.

230 **3.4 Crystallographic textures and seismic properties**

231 **3.4.1 Crystallographic textures**

232 The MTEX toolbox has been used to determine and represent the crystallographic
 233 textures and the J-index from EBSD data (Hielscher and Schaeben, 2008; Mainprice et al.,
 234 2011). The J-index quantifies the fabric strength and is dimensionless. It results from the
 235 integration of the density of the Orientation Distribution Function (ODF, $f(g)$) at a g orientation
 236 over the entire volume (Ismail and Mainprice, 1998):

$$237 \quad J = \int f(g)^2 dg \quad (1)$$

238 where $dg = d\varphi_1 d\phi d\varphi_2 \sin\phi / 8\pi^2$ and φ_1 , ϕ and φ_2 are the Euler angles, which represent the
 239 orientation of a crystal within the sample reference frame. $J = 1$ for a random distribution of
 240 the crystallographic axes, while J is infinite for single crystal orientation.

241

242 **3.4.2 Seismic properties**

243 We use the AnisEulerSC program to model the seismic properties of the Pello Hill
 244 mantle xenoliths. It allows us to consider the presence of different mineral phases, the
 245 crystallographic preferred orientations, and the presence of fluid and melt inclusions (Kim et
 246 al., 2020). AnisEulerSC is an extended version of the MTEX program (Hielscher and Schaeben,
 247 2008; Mainprice et al., 2011) which uses the CPO of the major phases (measured with EBSD),
 248 their respective modal content, and the stiffness tensor for each phase. In addition, the
 249 AnisEulerSC program considers the grain mean aspect ratio and the grain volume for the

250 seismic property computation (Kim et al., 2020) (see Supplementary Material 2 for
 251 comparison between MTEX and AnisEulerSC velocities for two very contrasting compositions).
 252 It is important to note that the elastic tensor of the aggregate varies as of function of the grain
 253 aspect ratio (Koch et al., 2004). AnisEulerSC also offers the possibility to consider oriented
 254 cracks that can be filled with crystallized minerals or fluids. It is based on the introduction of
 255 elastic inclusions into a background medium and the calculation of the average Self-Consistent
 256 (SC) elastic tensor (Eshelby, 1957; Hill, 1965) from the individual stiffness tensor of the fluid
 257 or the different minerals in the aggregate. For this method, each component is considered as
 258 an isolated inclusion in an infinite isotropic homogeneous background medium (Berryman and
 259 Berge, 1993).

260 For our study, we consider the stiffness tensors at a confining pressure of 2 GPa and
 261 ambient temperature. The 2 GPa pressure matches the mean depth (between 40 and 90 km
 262 depth) of the mantle xenoliths used in this study. The temperature effect was not
 263 implemented in the stiffness tensor due to the lack of experimental temperature derivatives
 264 for phlogopite and amphibole. The stiffness tensors used in the calculations are from
 265 Abramson et al. (1997) for olivine, Sang and Bass (2014) for diopside (clinopyroxene), Chai et
 266 al. (1997) for orthopyroxene, Peng and Mookherjee (2020) for amphibole, Chheda et al. (2014)
 267 for phlogopite and Da Silva et al. (1999) for ilmenite. The magnetite stiffness tensor of
 268 Reichmann and Jacobsen (2004) was used instead of chromite (which was indexed as
 269 magnetite in EBSD) because we found no pressure derivatives for chromite in the literature.
 270 Moreover, the chromite phase is present in a small amount, so the expected impact on the
 271 calculated velocities should be negligible. We corrected the effect of temperature on
 272 velocities for vein-free and crystallized vein-bearing peridotites aggregate (Table 1 and Table
 273 2, respectively) by applying a percentage decrease. This latter was calculated by using the
 274 velocity variation between a peridotite at 2 GPa/ambient temperature and 2 GPa/1200°C. At
 275 1200°C, the mean average velocities decrease is 7% for $V_{p_{max}}$, 9% for $V_{p_{min}}$, 10% for $V_{s1_{max}}$,
 276 and 11% for $V_{s1_{min}}$, $V_{s2_{max}}$ and $V_{s2_{min}}$ (Supplementary Material 3).

277 We first determined the velocities of all the xenoliths (peridotite or peridotite + vein)
 278 by computing the SC tensor in only one step (Figure 4). For the computation, we use the elastic
 279 tensor, a mean measured aspect ratio, and an ellipse approximation for each mineral. To
 280 consider the orientation of veins in the mantle xenoliths, we then determined the velocity by
 281 computing the average SC tensor in two or three steps, considering fluid-filled or crystalline
 282 veins, respectively, for 4 vein-bearing samples (PH4, PH9, PH18 dunites, and PH27
 283 harzburgite). For peridotite with crystalline veins, we compute 1) the vein-free peridotite
 284 average SC tensor, 2) the crystallized vein average SC tensor, and 3) the average peridotite +
 285 vein SC tensor for a given vein orientation. In the final step (3), to obtain only the mean SC
 286 tensor of the peridotite (without orientation), the peridotite minerals are defined as spheres
 287 while we approximate the vein minerals by ellipses. For the fluid-filled veins, we omit the
 288 second step (SC tensor of the vein) as the fluid bulk moduli are known from experimental
 289 density measurements (Genge et al., 1995; Sakamaki et al., 2011, 2010, 2009).

290 Finally, the velocities are calculated in all directions from the average SC tensor using the
 291 equation from (Christoffel, 1877) which relates the elastic stiffness tensor with V_p , V_{s1} , V_{s2} ,
 292 and the anisotropy. The anisotropy (AV) is computed as followed:

$$293 \quad AV = 200 \times \frac{V_{max} - V_{min}}{V_{max} + V_{min}} \quad (2)$$

294 where V_{max} is the maximum velocity and V_{min} the minimum velocity for V_p or V_{s1} or V_{s2} in the
295 sample.

296

297 **4 Pello Hill mantle xenoliths**

298 **4.1 Texture and mineralogy**

299 Pello Hill mantle xenoliths are refractory vein-free and vein-bearing harzburgite and
300 dunite with coarse granular to porphyroclastic textures with subequant to tabular olivine and
301 pyroxene grains (0.1–5 mm) (Table 1, Table 2). Some of the largest olivine crystals are
302 elongated, with shape ratios up to 1:10. Their shape-preferred orientation marks the foliation.
303 These large crystals usually display undulose extinction and subgrain boundaries suggesting
304 deep and intracrystalline deformation (Passchier and Trouw, 2005). Orthopyroxenes (2 to 20
305 modal percent in dunite and harzburgite, respectively) present either exsolution of
306 clinopyroxene, amphibole inclusions, or clinopyroxene growth at rims (Figure 2.a).
307 Clinopyroxenes in peridotites (out of the vein) are scarce, occur as isolate interstitial crystals
308 with curved margins (Figure 2.b), and can be associated with phlogopite and amphibole small
309 interstitial grains, or as inclusions. Phlogopites and/or amphiboles are present as interstitial
310 “patches”, sometimes associated with clinopyroxenes (Figure 2.c and d). Some patches
311 contain spinels with no coronitic reaction. Oxides can be found as inclusions in clinopyroxene
312 and phlogopite (Figure 2.c and d) or interstitial in the peridotite (Figure 2.b). Some interstitial
313 sulfurs are also present within the peridotites.

314 In the vein-bearing xenoliths, the vein proportion ranges from 6% (PH18) up to 100%
315 (PH23) of the thin section (Table 1). The rims of the vein are well-defined with large crystals
316 (Figure 2.f) or diffuse with small interstitial grains (crystals with 500-2100 μm in size in the
317 center of the vein and 80-150 μm in size at the rim; Figure 2.e). Veins comprise an assemblage
318 of clinopyroxene, phlogopite, amphibole, and oxide (Figure 2.e, f and h). The proportions of
319 clinopyroxene, phlogopite, amphibole, and oxide vary from (Table 1): high proportion of
320 clinopyroxene (40-60%) and low proportion of amphibole (12-17%) (PH4 and PH18) to high
321 amphibole (41-52%) and low clinopyroxene (19%) and phlogopite (18-22%) proportions (PH9
322 and PH27). PH23 xenolith is a hornblendite with amphibole (46%), phlogopite (20%),
323 clinopyroxene (17%), and interstitial olivine (16%) (Figure 2.g).

324

325 **4.2 Mineral composition**

326 **4.2.1 Olivine**

327 Olivines are Mg-rich with Mg# ($=\text{Mg}/(\text{Mg}+\text{Fe}^{2+})\times 100$) ranging from 87.7 (PH4) to 93.1
328 (PH18) in vein-bearing peridotites, and from 92.0 (PH26) to 93.1 (PH13) in vein-free
329 peridotites. Olivines from PH18 dunite have a Mg# gradient with Mg# decreasing approaching
330 the metasomatic vein (89.5 near the vein and 93.1 far from the vein). Olivines in veins (PH23)
331 have low NiO and SiO₂ contents (0.1-0.2 wt.% and 38.5-39.7 wt.%, respectively) and low Mg#

332 (77.5 to 79.6) compared to olivine in peridotites (0.3-0.5 wt.% NiO, 40.9-42.1 wt.% SiO₂ and
333 Mg# = 87.7-93.1; Supplementary Material 4).

334

335 **4.2.2 Pyroxenes**

336 Orthopyroxenes, present in most of peridotites, are enstatites (Supplementary
337 Material 4). Orthopyroxenes in the vein-bearing samples have a lower Mg# (<92), i.e. higher
338 concentrations in FeO (> 5 wt.%) and lower concentrations in MgO (< 35 wt.%) compared to
339 vein-free peridotites (Mg# = 92.4-93.8).

340 Clinopyroxenes have diopside/augite compositions (Wo₄₅En₅₁Fs₄ to Wo₃₃En₆₃Fs₄).
341 Clinopyroxenes are diopsides in the veins and vein-bearing peridotites (PH4, PH9, PH18,
342 PH23), and are augite in the vein-free samples (PH1, PH13, PH17, PH26). Compared to
343 clinopyroxene in peridotites, the clinopyroxenes in veins are enriched in CaO (21-23 wt.%,
344 Figure 3.a) and depleted in Cr₂O₃ (< 1 wt.% in vein and 1.5-4 wt.% out of vein, Supplementary
345 Material 4). In the vein-bearing samples (PH4, PH9, and PH18), there is a chemical gradient
346 from the vein to the peridotite from 0.02 up to 3.0 wt.% for Cr₂O₃ and from 22.7 to 19.2 wt.%
347 for CaO (Figure 3.a). In the dunite sample (PH4), the core of clinopyroxenes in the veins have
348 0.03-0.17 wt.% of Cr₂O₃ and 22.0-22.7 wt.% of CaO, whereas near the vein, Cr₂O₃ and CaO
349 concentrations in clinopyroxene core are 2.4-2.5 wt.% and 21.4 wt.%, respectively. In the
350 dunite, far from the vein, clinopyroxenes have 2.9-2.9 wt.% of Cr₂O₃ and 21.2-21.3 wt.% of
351 CaO (Figure 3.a). All clinopyroxenes are unzoned except in dunite sample PH4 with Cr₂O₃
352 ranging from 2.4-3 wt.% in the core down to 1.6-2.1 wt.% at the rims. The vein-bearing dunite
353 PH9 has clinopyroxenes in the peridotite with a large variation in Cr₂O₃ concentrations (from
354 0.7 to 2.4 wt.%). These clinopyroxenes with the lowest Cr₂O₃ values have similar
355 concentrations to clinopyroxenes occurring within the veins (Supplementary Material 4).

356

357 **4.2.3 Amphibole**

358 The amphiboles are calcium-rich (8.8-11.0 wt.% CaO) with Mg# ranging from 77.8
359 (vein sample, PH23) up to 93.4 (vein-free sample, PH13) (Figure 3.b and c). Most of them are
360 edenite (Leake et al., 1997). Only rare amphiboles in veins from sample PH4 and PH23 are
361 classified as pargasite.

362 Amphiboles present in veins or as interstitial minerals in peridotites (further called
363 "patch amphibole") are chemically distinct. Three chemical groups can be defined: i) vein-free
364 samples and a PH18 patch (lowest vein proportion, 6%) contain amphiboles with FeO < 3.1
365 wt.%, Mg# > 91, TiO₂ < 1.5 wt.%, CaO < 9.5 wt.% and Na₂O > 4 wt.%, ii) amphiboles from veins
366 and PH4 and PH9 (22% and 62% vein bearing peridotites) patches have 3.1 wt.% < FeO < 6 wt.%,
367 85 < Mg# < 91, TiO₂ > 2 wt.%, CaO > 9.7 wt.% and Na₂O < 4 wt.%, iii) PH23 (hornblendite)
368 amphiboles have FeO > 7 wt.%, Mg# < 85 and TiO₂ > 2.5 wt.% (Figure 3.b, c and Supplementary
369 Material 4).

370

371 4.2.4 Phlogopite

372 In the Pello Hill xenoliths, there are at least two chemical groups of phlogopite. These
373 within patches have concentrations of $\text{TiO}_2 \leq 2$ wt.%, $\text{Cr}_2\text{O}_3 > 2$ wt.%, $\text{Mg\#} > 92$, and $\text{K}_2\text{O} < 9$
374 wt.%, whereas phlogopites in veins have $\text{TiO}_2 > 3$ wt.%, $\text{Cr}_2\text{O}_3 < 1$ wt.%, $\text{Mg\#} < 92$ and $7.2 <$
375 $\text{K}_2\text{O} < 8.6$ wt.% (Figure 3.d, and Supplementary Material 4). The phlogopites in the vein sample
376 PH23 have a very low Mg# (80.6-81.8) compared to other phlogopites in vein from other Pello
377 Hill xenoliths ($\text{Mg\#} > 88$) (Figure 3.d).

378

379 4.2.5 Oxides

380 Two distinct types of oxides are present in the Pello Hill xenolith samples: chromite
381 and ilmenite. Chromites are present in the peridotites or in the metasomatic vein edges. They
382 are interstitial or occur as inclusions in phlogopite, amphibole, and less frequently in
383 clinopyroxene (Figure 2.b, c and d). Ilmenites are only interstitial in the metasomatic veins
384 (PH9 sample, Figure 2.h). The concentration of Cr_2O_3 in chromites ranges from 47 to 60 wt.%.
385 Chromites at the rim of the veins have higher titanium (> 2.5 wt.% TiO_2) and lower chromium
386 concentrations (< 50 wt.% Cr_2O_3) than those located farther within the peridotite (0.05-1.9
387 wt.% TiO_2 and 53.2-60.2 wt.% Cr_2O_3). The titanium concentration is higher in the interstitial
388 chromites (0.5 and 1.6 wt.% TiO_2 in PH26 and PH9, respectively) and chromium content is
389 higher in chromites occurring as inclusions (1.5 and 2 wt.% Cr_2O_3 in PH26 and PH9,
390 respectively) (Supplementary Material 4).

391

392 4.3 Microstructures

393 In the vein-free xenolith, some of the largest olivine porphyroclasts are elongated,
394 parallel to the olivine [100] axis. The subgrain boundaries (undulose extinction) are
395 perpendicular to the olivine [100] axis (Supplementary Material 5). The olivine J-index ranges
396 from 4.00 to 4.79 (Supplementary Material 5). These values are in the lower range of the J-
397 index estimated for worldwide natural olivine aggregates (between 3.2 and 27.0) by (Ismail
398 and Mainprice, 1998).

399 The four peridotite samples with veins have a vein orientation oblique or
400 subperpendicular to the olivine [100] axis (Figure 4). There is no preferential orientation of
401 clinopyroxene, amphibole, and phlogopite in veins, even if the amphibole [001] axis of PH9
402 and PH4 seems to be parallel to the olivine [100] axis.

403 For almost all Pello Hill samples, vein sample PH23 and peridotite PH27 with 80% vein
404 excluded, the olivines have a marked orientation with a point pattern for the [100] axis, and a
405 girdle pattern for [010] and [001] axes (Figure 4 and Supplementary Material 5).

406 The aspect ratios of the main phases (olivine, orthopyroxene, clinopyroxene,
407 amphibole, phlogopite) used for velocity computation correspond to the mean aspect ratio,
408 which is the measured mean longest axis divided by the mean shortest axis. For the full
409 aggregate (peridotite or peridotite + vein) velocity computation, the mean aspect ratios

410 calculated from all measured samples are: 1:1.6:1 for olivine, 1.6:1:0.6 for orthopyroxene and
 411 clinopyroxene, 1:1.7:1 for amphibole, 0.6:1:2 for phlogopite, 1:1:1 for magnetite and 1:1:2.8
 412 for ilmenite. For the seismic properties of oriented veins, we used the average aspect ratio for
 413 clinopyroxene, amphibole, and phlogopite (1.7:1:1).

414

415 **5 Seismic properties of mantle xenoliths**

416 **5.1 Mantle peridotites**

417 In harzburgites PH13 and PH27, and dunites PH8 and PH26, the foliation is marked
 418 by olivine elongation, with lineation sub-parallel to [100] axes and a girdle distribution of [010]
 419 axes perpendicular to the foliation. The fast and slow V_p follow the [100] and [010] olivine
 420 axes, respectively, indicating that olivine controls the velocity amplitude and orientation
 421 (Supplementary Material 5 and Table 2). The fast and slow V_{s1} are along [101] and a
 422 combination of [001] and [100] axes, respectively. V_{s2} presents its maximum along [100] and
 423 its minimum for a combination of [001] and [010] axes, respectively. All vein-free samples
 424 have millimetric olivine with sub-grains. The fast velocities (V_p , V_{s2}) are parallel to the olivine
 425 porphyroclast elongation (Supplementary Material 5, unbroken lines on V_p plots).

426 Except for the dunite PH8 which exhibits lower velocities ($V_p=6.9-7.7 \text{ km}\cdot\text{s}^{-1}$ and V_{s1}
 427 $=4.1-4.3 \text{ km}\cdot\text{s}^{-1}$, and $V_{s2} = 4.0$ to $4.1 \text{ km}\cdot\text{s}^{-1}$), all vein-free samples and samples with low vein
 428 proportions (<22%) have homogeneous velocities with $V_{p_{\min}}$ ranging from 7.3 to $7.5 \text{ km}\cdot\text{s}^{-1}$,
 429 $V_{p_{\max}}$ from 8.4 to $8.5 \text{ km}\cdot\text{s}^{-1}$, $V_{s1_{\min}}$ from 4.3 to $4.4 \text{ km}\cdot\text{s}^{-1}$, $V_{s1_{\max}}$ from 4.5 to $4.6 \text{ km}\cdot\text{s}^{-1}$, $V_{s2_{\min}}$
 430 from 4.1 to $4.2 \text{ km}\cdot\text{s}^{-1}$, and $V_{s2_{\max}}$ from 4.3 to $4.4 \text{ km}\cdot\text{s}^{-1}$ (Table 2). The lower velocities and
 431 maximum V_p/V_s ratio for PH8 are most probably due to the presence of interstitial
 432 phlogopite/amphibole (7.8%).

433

434 **5.2 Clinopyroxene, phlogopite, amphibole-bearing mantle veins**

435 In all clinopyroxene, phlogopite, amphibole-bearing mantle veins, the fast and slow
 436 velocity directions follow the amphibole axes ([001] and [100] axes, respectively). However,
 437 when the proportion of phlogopite is higher than amphibole, the phlogopite also partly
 438 controls the fast ([100] and [010] axes) and the slow ([001] axis) velocities (Supplementary
 439 Material 6).

440 For all mineral assemblage (clinopyroxene, amphibole, and phlogopite), the
 441 computed velocities of the veins at 2 GPa and 1200°C are similar and vary from 3.3 to $5.5 \text{ km}\cdot\text{s}^{-1}$
 442 for V_p , 2.4 to $3.1 \text{ km}\cdot\text{s}^{-1}$ for V_{s1} , and 2.2 to $2.7 \text{ km}\cdot\text{s}^{-1}$ for V_{s2} (Supplementary Material 6). It
 443 should be noted that there is no clear correlation between velocities and relative phase
 444 proportion of amphibole, phlogopite, and clinopyroxene. The velocity of veins is always lower
 445 than the velocities of peridotites.

446

447 5.3 Mantle peridotites and veins

448 For the peridotite containing a low vein proportion (PH18, 6% of vein), the presence
 449 of the vein in the peridotite decreases the mean velocity from 8.4-7.4 to 8.2-7.1 km.s⁻¹ for V_p,
 450 and from 4.5-4.1 to 4.4-4.0 km.s⁻¹ for V_s. This corresponds to a decrease by 2-4% V_p and 2-
 451 3% V_s compared to the peridotite (PH18, Figure 4 and Table 2). However, the velocity
 452 orientation is still controlled by the olivine orientation (Figure 4).

453 In peridotite containing 22% of veins (with 17-18% of phlogopite/amphibole), the
 454 presence of the veins causes a mean decrease of the velocity from 8.5-7.4 to 7.6-6.5 km.s⁻¹ for
 455 V_p and from 4.6-4.1 to 4.1-3.7 km.s⁻¹ for V_s. That corresponds to a decrease by 10-12% V_p and
 456 9-10% V_s compared to the peridotite (PH9, Figure 4 and Table 2). This vein proportion initiates
 457 a shift of the velocity directions, and the slowest V_p direction does not follow the olivine [010]
 458 axis. The veins and peridotite + vein minimum velocities almost have the same orientation
 459 suggesting that the slowest velocities are controlled by the vein velocity tensor
 460 (Supplementary Material 6 and Figure 4, respectively) and the vein orientation.

461 Compared to the peridotite, peridotites with 62% and 80% of veins (PH4 and PH27)
 462 generate a mean decrease in the velocity from 7.5-7.2 to 4.5-4.6 km.s⁻¹ and from 8.4-8.3 to
 463 6.0-5.4 km.s⁻¹ for V_{p_{min}} and V_{p_{max}} (-38 to -40% and -29 to -35%, respectively), from 4.4-4.1 to
 464 2.9-3.1 km.s⁻¹ and from 4.6-4.3 to 3.0-3.4 km.s⁻¹ for V_{s_{min}} and V_{s_{max}} (-29 to -31% and -25 to -
 465 31%, respectively) (Figure 4 and Table 2). With 60% of phlogopite/amphibole vein assemblage,
 466 the velocity direction completely shifts away from the main-driving-velocity olivine axes
 467 (Figure 4, PH4).

468 In the vein-rich samples, the maximum and minimum V_p of the full sample follow the
 469 orientations of amphibole ([001] and [100] axes respectively) and clinopyroxene ([001] and
 470 [010] axes, respectively) (Figure 4 and Supplementary Material 6). The V_p fast and slow axes
 471 of phlogopite ([010], [100] and [001]) are overwritten by the slow and fast axes of the
 472 amphibole, respectively. The fast V_{s₁} mostly follows an intermediate direction between the
 473 amphibole ([001]) and the phlogopite ([100]) axes. The slow V_{s₁} is oriented parallel to the slow
 474 V_p, while the fast V_{s₁} is uniformly oriented perpendicular to the slow V_{s₁}. The fast V_{s₂} is
 475 oriented parallel to the fast V_p, while the slow V_{s₂} is uniformly oriented perpendicular to the
 476 fast V_p (Supplementary Material 6).

477 The main direction of the velocity also depends on the vein orientation (Kim et al.,
 478 2020 and Supplementary Material 7). The maximum of V_p and V_{s₂} velocities are perpendicular
 479 (PH4, PH27) or oblique/sub-perpendicular to the orientation of the veins (PH18, PH9, Figure
 480 4). The vein orientation follows the main orientation of the olivine [010] axis for a vein
 481 proportion < 60%.

482

483 5.4 Fluid-veins in mantle peridotite

484 The composition of lavas from the NTD ranges from H₂O-CO₂-rich sub-alkaline to
 485 highly alkaline magmas attesting of complex fluid/melt compositions within the lithospheric
 486 mantle (Baudouin and Parat, 2020; De Moor et al., 2013; Lee and Rudnick, 1999; Lee et al.,
 487 2017; Mana et al., 2015, 2012; Muirhead et al., 2020). To account for the variable geochemical

488 composition of magmas and fluid percolation in the mantle, we determined the seismic
 489 properties of the mantle for vein-bearing peridotite considering different vein orientations
 490 relative to the olivine CPO, and 4 different melt compositions. These melts are: a dry
 491 peridotitic melt, used as a reference for dry basalt, a CaCO_3 fluid, which refers to carbonatitic
 492 melt, a hydrous peridotitic melt and a CO_2 -bearing peridotitic melt (Table 4; Genge et al., 1995;
 493 Sakamaki et al., 2011, 2010, 2009).

494 First, we use AnisEulerSC to calculate the elastic tensor of the peridotite at 2 GPa and
 495 1200°C, with mineral proportion, CPO and aspect ratio, as performed for crystallized vein-
 496 bearing peridotites (step 1). Then, the tensor of the whole aggregate with fluid-filled
 497 inclusions (high pressure and high temperature) is computed from the peridotite elastic tensor
 498 and an isotropic fluid tensor. The fluid tensor is defined by the bulk modulus of the fluid (Table
 499 4; Genge et al., 1995; Sakamaki et al., 2011, 2010, 2009). We fix the aspect ratio of the
 500 inclusions 5:1:5 (lens shape) to model an intermediate geometry between an isolated melt
 501 pocket and interconnected pores filled with melt (intergranular melt; Clark and Lesher, 2017).
 502 These are the usual shapes of the first liquids observed in partial melting experiments
 503 (Hammond and Humphreys, 2000).

504 The seismic properties of PH4 and PH27 cannot be fully modeled with fluid-filled
 505 inclusions because the vein proportion is too large and prevents the Vs from propagating
 506 (calculated Vs < 0.2 km.s⁻¹). In these samples, it induces unrealistic Vp/Vs (above 18) and P-
 507 waves velocities are reduced to less than 3 km.s⁻¹.

508

509 **5.4.1 Orientation of the fluid-filled inclusions in peridotite**

510 Three lens-shape inclusion orientations have been chosen relative to the structural
 511 frame (X,Y,Z) of the host peridotite PH9 (Figure 5 and Supplementary Material 7), defined
 512 following the observation of the foliation plane (X,Y) and lineation (X). The fastest velocities
 513 have orientations parallel to directions that combine the longest axes of the inclusions (A1)
 514 and the maximum velocity of the host rock, i.e., parallel to the [100] axis of olivine. For
 515 instance, peridotite with 5:5:1 oriented inclusions displays higher maximum velocity than the
 516 peridotite with 1:5:5 orientations, where the long axis of the inclusions is perpendicular to the
 517 [100] axis of olivine.

518

519 **5.4.2 Velocities for different fluid compositions in lens shape inclusions**

520 For lens-shaped fluid-filled inclusions, the velocities and Vp/Vs ratios vary as a
 521 function of fluid composition and aspect ratio for H_2O and CaCO_3 composition (Kendall, 2000;
 522 Mainprice, 1997 and Table 3). The velocities and Vp/Vs ratios for CO_2 -bearing peridotitic melt
 523 (2.5% of CO_2) and anhydrous peridotitic melt are very similar, with velocity variations lower
 524 than 0.05 km.s⁻¹.

525 For CaCO_3 melt and 6% of lens-shape inclusions (PH18), only Vp has a significant
 526 change compared to the anhydrous inclusions (+0.09, +0.23 km.s⁻¹ compared to dry melt,
 527 equivalent to +1% and +3.4% respectively, Table 3). When the inclusion proportion in the

528 sample is 22% (PH9), the velocities variations do not have the same trend: $V_{p_{\max}}$ increases by
 529 0.07 km.s^{-1} (+1%) while $V_{p_{\min}}$ decreases by 0.12 km.s^{-1} (-2%) compared to dry melt.

530 For hydrous lens-shape inclusions (5 wt.% water in the melt), there is an important
 531 decrease of V_p compared to anhydrous melt: down to -0.32 km.s^{-1} (equivalent to -5%) when
 532 6% of inclusions is present in the sample, and down to -0.85 km.s^{-1} (equivalent to -16%) when
 533 there is 22% of inclusions (Table 3). The maximum velocity of V_{s_2} is also significantly impacted
 534 with a decrease of -0.16 km.s^{-1} (-5% of variation) with 22% of inclusions.

535

536 6 Discussion

537 6.1 Depth of fluid/melt-rock interaction and geotherm beneath the NTD

538 Characterizing the deep asthenospheric mantle source of alkaline magmas is crucial
 539 because it represents the source of the metasomatic agent leading to the formation of veins
 540 within the lithospheric mantle. In the southern part of the NTD, the Labait and Pello Hill
 541 volcanoes erupted CO_2 -rich nephelinites and melilitites with very close trace element
 542 composition (Baudouin and Parat, 2020; Dawson and Smith, 1988) suggesting the presence of
 543 a deep phlogopite-carbonate-garnet-bearing source beneath the Lithosphere Asthenosphere
 544 Boundary (LAB > 120 km, Baudouin and Parat, 2020; Lee and Rudnick, 1999). Labait volcano
 545 carried garnet-bearing xenoliths, whereas at Pello Hill volcano, only spinel-peridotite xenoliths
 546 have been sampled. This either suggests a shallower depth of partial melting for highly alkaline
 547 parental magmas as observed for the Natron-Engaruka volcanoes (75-90 km, Mattsson et al.,
 548 2013), or that melilitite magma did not sample garnet-bearing xenoliths because of different
 549 mantle rheology or lower volume of magmas. The few experimental studies carried out at
 550 lithospheric conditions (up to 3 GPa, e.g. Condamine et al., 2016) do not allow to estimate the
 551 depth of partial melting of peridotite that leads to the formation of alkali magmas. Only one
 552 empirical equation has been calibrated for partial melting producing basaltic melts, based on
 553 the SiO_2 and MgO contents of the primary melts (Albarède, 1992). Using this empirical
 554 equation and the composition of Pello Hill melilitite ($\text{CaO}+\text{Na}_2\text{O}+\text{K}_2\text{O} = 16.34 \text{ wt.}\%$, $\text{SiO}_2+\text{Al}_2\text{O}_3$
 555 $= 47.61 \text{ wt.}\%$, Supplementary Material 9), we propose a melting pressure of 5.3 GPa (175 km).
 556 This depth is located below the estimated LAB beneath the NTD from surface wave
 557 tomography (Craig et al., 2011; Fishwick, 2010; Priestley et al., 2008), and is deeper than the
 558 CO_2 -free partial melting experiments (e.g., Adam, 1990; Condamine et al., 2016; Foley et al.,
 559 2012; Frey et al., 1978; Green and Falloon, 1998). It corroborates however the deep origin of
 560 magma and mantle xenoliths beneath the NTD (this study, and Lee and Rudnick, 1999).

561 The depth and temperature we estimated from mineral equilibrium in the vein-free
 562 peridotites from Pello Hill suggest that xenoliths originate from $\sim 37 \text{ km}$ (PH4, dunite) down
 563 to 150 km depth (PH13, harzburgite), with temperatures ranging from 1040 to 1200°C (Figure
 564 6, Supplementary Material 8). Spinel-phlogopite-bearing Pello Hill Iherzolites (PH17, PH26)
 565 originate from 82 to 91 km depth (Figure 6). In contrast, mineral equilibrium in the vein-free-
 566 and spinel-bearing harzburgite (PH13, 150 km) indicates deeper mantle origin although garnet
 567 was not observed in the xenoliths. The P-T conditions agree with the stability field
 568 experimentally determined for phlogopite, extended for 1100-1350°C and 3-6 GPa (90-180
 569 km) (Condamine et al., 2016 and Condamine personal communication). The P-T conditions are

570 close to or just above the stability field of spinel in CMAS or MAS experiments (up to 180 km
571 in the harzburgitic mantle, e.g., Klemme, 2004; Ziberna et al., 2013). However, it should be
572 noted that the presence of phlogopite and carbon may influence the experimental barometer
573 calibration determined by Brey and Köhler (1990) and Köhler and Brey (1990) for garnet
574 lherzolite.

575 It was not possible to estimate the depth for most vein-bearing xenoliths because
576 either (i) there is no orthopyroxene in the samples (PH23) or (ii) the chemical equilibrium
577 between orthopyroxene and clinopyroxene or olivine and clinopyroxene was not reached
578 (PH1, PH23).

579 The NTD deep mantle xenoliths (> 100 km) display estimated temperatures
580 consistent with the plume-modified geotherm (Figure 6) (Gibson and McKenzie, 2023; Selway
581 et al., 2014). This is in accordance with several geophysical and geochemical studies, and the
582 presence of a mantle plume upwelling below the Tanzanian Craton and the NTD (Clutier et al.,
583 2021; Huerta et al., 2009; MacDonald et al., 2001; Mulibo and Nyblade, 2013a; Pik et al., 2006;
584 Tiberi et al., 2019; Weeraratne et al., 2003). Shallower lithospheric xenoliths (< 100 km) exhibit
585 higher temperatures than the plume-modified geotherm, ranging from 1040°C to 1200°C
586 (Figure 6). The overall P-T distribution of NTD mantle xenoliths cannot be simply explained by
587 Cenozoic, Proterozoic, cratonic or even mantle plume-modified geotherms (Artemieva, 2009;
588 Selway et al., 2014). The Pello Hill mantle xenoliths rather follow a 1100°C isotherm, near the
589 carbonated peridotite solidus (Dasgupta et al., 2013), and most likely relates to the volatile-
590 bearing peridotite solidus and crystallization temperatures of phlogopite and amphibole. This
591 is in accordance with the presence of CO₂-rich silicate magmas and carbonatites in the region
592 (Dawson and Smith, 1988; De Moor et al., 2013; Muirhead et al., 2020).

593

594 **6.2 Lithospheric mantle geochemical evolution**

595 The presence of veins in mantle xenoliths attests to extensive metasomatism
596 beneath the NTD. Both modal abundances and chemical signatures strongly suggest the
597 occurrence of one or several metasomatic event(s) (Aulbach et al., 2011; Chesley et al., 1999;
598 Cohen et al., 1984; Koornneef et al., 2009; Lee and Rudnick, 1999; Rudnick et al., 1994). In the
599 southern part of the NTD (Labait volcano), few veins have been observed in mantle peridotites
600 (Koornneef et al., 2009; Vauchez et al., 2005) and only a few spinel-peridotites display
601 interstitial phlogopite, suggesting weak modal metasomatism. On the contrary, in the
602 northern part, the Pello Hill xenoliths provide evidence of intense metasomatic events at
603 relatively shallow depths (40-90 km) (Aulbach et al., 2011; Koornneef et al., 2009; this study).

604 The mineral assemblages and composition of veins in the Pello Hill xenoliths (e.g., Fe
605 and Ti-rich ilmenite, low-Cr₂O₃ and high-TiO₂ diopside, phlogopite and amphibole, this study)
606 indicate the presence of FeO- and TiO₂-rich alkaline mafic silicate melts/fluids within the
607 lithospheric mantle. Those melts/fluids are also CaO-rich, as evident from the high CaO
608 concentrations in clinopyroxenes and amphiboles from veins or vein-bearing xenoliths (Figure
609 3). In addition, amphiboles in the veins are potassium-rich, which may be interpreted as the
610 imprint of a subduction-related fluid (e.g., Soltanmohammadi et al., 2018).

611 We also observed chemical variations between the core and rim of minerals, and
612 depending on the distance from the vein. Orthopyroxenes are zoned with higher Al_2O_3 and
613 Cr_2O_3 concentrations in the core than in the rim indicating that the enstatite either re-
614 equilibrated at the rim with a circulating fluid or melt, or that the core of minerals crystallized
615 deeper than the rim (Longhi et al., 1993). The decrease of Cr_2O_3 concentration observed in
616 clinopyroxenes of PH4 dunite from the core (2.4-3 wt.%) to rim (1.6-2.1 wt.%) also argues for
617 metasomatic fluid/melt circulation and re-equilibration of the minerals. In addition, the
618 chemical gradient observed for clinopyroxene and olivine from the vein to the peridotite may
619 result from a diffuse metasomatic percolation within the whole rock mantle peridotite
620 associated to the metasomatic veins (Bodinier et al., 1990). Furthermore, a higher proportion
621 of veins may indicate a higher volume of melt within the peridotite as well as a longer time of
622 percolation and re-equilibration between host-peridotite and alkaline melt (e.g., low NiO in
623 olivine for vein proportion > 50%, PH4).

624 The presence of harzburgites with no or rare phlogopites and amphiboles (PH1 and
625 PH2, Table 1) indicates that such a refractory lithospheric mantle below Pello Hill underwent
626 melt extraction, and may be linked to subduction magmatism (Archean, Proterozoic?) or
627 recent intraplate magmatism (Aulbach et al., 2011; Rudnick et al., 1994). On the other hand,
628 harzburgites with interstitial phlogopites or amphibole patches (PH13, PH18 and PH24), and
629 2-10% clinopyroxene-rich PH8 and PH26 dunites, suggest later re-fertilization processes
630 associated with metasomatic events. The interstitial metasomatic phlogopites and
631 amphiboles are often associated with chromite with no coronitic reaction, suggesting that the
632 presence of "primary" spinel may favor phlogopite and/or amphibole growth during
633 metasomatic event. These patches of minerals are MgO , Cr_2O_3 and Na_2O -rich compared to
634 those occurring within the veins. These new minerals were formed during a metasomatic
635 event involving hydrous and potassic fluids/melts. These fluids may be subduction-related
636 before the Mozambique Belt orogen (Aulbach et al., 2011; Rudnick et al., 1994) or may be
637 more recent and plume-related, with intermediary composition between carbonatitic and
638 silicic (Aulbach et al., 2011; Bell and Simonetti, 1996; Mollet et al., 2009). Further studies,
639 especially isotopic dating, would help to decipher between the metasomatic event(s) and
640 long-term re-equilibration below Pello Hill (e.g., Koornneef et al., 2009).

641

642 **6.3 Seismic properties of metasomatized lithospheric mantle**

643 **6.3.1 Seismic properties of crystallized-vein lithospheric mantle**

644 In the Pello Hill mantle peridotites, the foliation is marked by the elongation of olivine
645 porphyroclasts parallel to the [100] axis, and the veins crosscut the foliation (perpendicular to
646 oblique to the olivine [100] axis) (Figure 4 and Baptiste et al., 2015). The fast and slow V_p
647 follow the [100] and [010] olivine axes, respectively, indicating that olivine controls the
648 velocity amplitude and orientation (the fast velocity V_p being parallel to [100] axis). The
649 presence of weak modal metasomatism (8% interstitial phlogopite and amphibole, PH8)
650 decreases V_p by about 7 to 9%, V_{s1} by 6%, and V_{s2} by 4 to 5% compared to vein-free
651 peridotites (Figure 4 and Table 2). Still, it does not modify the velocity orientation, that is
652 controlled by the olivine orientation (CPO).

653 The computed velocities for vein-bearing peridotites clearly indicate that the
654 proportion of metasomatic minerals (clinopyroxene, amphibole, and phlogopite) decreases
655 V_p and V_s , with phlogopite being the most effective mineral, followed by amphibole and then
656 clinopyroxene (Figure 4, Table 1 and Table 2), in agreement with single crystal seismic
657 properties (Almqvist and Mainprice, 2017). The presence of 22% of crystallized veins in the
658 peridotite decreases V_p by 10 to 12%, and V_{s_1} , and V_{s_2} by 9 to 10% (PH9, Figure 4). These
659 values are close to those previously determined for vein-bearing peridotite xenoliths from
660 Eledoi volcano using MTEX program (not considering grain volume) at ambient pressure and
661 temperature (28% of vein, Baptiste et al., 2015). However, the consideration of the grain
662 volume in AniseulerSC decreases the maximum velocities by 0.6 km.s^{-1} for V_p and V_{s_2} (-7%
663 and -12%, respectively) and 0.5 km.s^{-1} for V_{s_1} and (-12%) compared to Baptiste et al. (2015).
664 Importantly, when the vein-bearing peridotites is with $\geq 60\%$ of vein, the P-wave velocity
665 anisotropy is dominated by the velocity orientation of the vein, and no more by the main
666 olivine orientation (Figure 4).

667

668 6.3.2 Seismic properties of deep fluid/melt in the lithospheric mantle

669 The presence of fluid/melt in the lithospheric mantle beneath the NTD is strongly
670 supported by the presence of recently erupted magmas at the surface (Mana et al., 2015),
671 and by low velocity zones in tomographic images (Mulibo and Nyblade, 2013b; Tiberi et al.,
672 2019). Melt percolation is a deep (175 km, Pello Hill melilitite, Figure 6) and continuous
673 process leading to mantle-rock interactions and changes of mantle rheology. The volume,
674 distribution, and composition of melt may have important implications for the seismic
675 properties of the mantle (Clark and Lesher, 2017). In addition to melt fractions and aspect
676 ratio (Clark and Lesher, 2017; Kendall, 2000; Kendall et al., 2006), the mineralogical variations
677 (Stixrude and Lithgow-Bertelloni, 2005), the presence of volatile species (Karato and Jung,
678 1998), and the anelasticity enhanced by high temperatures (Faul and Jackson, 2005) may
679 contribute to lower seismic velocities.

680 The percolation of deep highly alkaline and alkaline magmas in the lithospheric
681 mantle beneath the NTD is supported by the occurrence of melilitites and nephelinites,
682 whereas the presence of carbonatite and CO_2 -rich and/or H_2O -rich melt inclusions in minerals
683 and hydrous minerals in magmas suggests a wide range of magma compositions (Baudouin et
684 al., 2018, 2016; Baudouin and Parat, 2020; Dawson, 2012; Guzmics et al., 2012).

685 Our computation of seismic properties of natural mantle xenoliths from Pello Hill
686 clearly indicates that the presence of melt and/or fluids in peridotitic rocks decreases both V_p
687 and V_s (Figure 4 vs Figure 5 and Table 2 vs Table 3). The presence of anhydrous peridotitic
688 melt in the crystallized peridotitic mantle would lower the P-velocity by 5 to 8% and S-velocity
689 by 4 to 10% for 6% of the melt fraction (peridotite + fluid/melt velocities in Table 3 and
690 peridotite velocity in Figure 4). This agrees with the elastic properties of silicate melts which
691 predict a P and S wave velocity decrease of up to 9 and 11%, respectively, for 1-5% of the
692 anhydrous melt between 70 and 150 km deep (Clark and Lesher, 2017).

693 Interestingly, the addition of 2.5 wt.% of CO_2 in anhydrous melt does not change the
694 seismic properties compared to anhydrous peridotitic melt (Table 3). However, the lack of

695 experimental determination of bulk modulus for higher CO₂ content at high pressure does not
696 allow evaluation of carbonate-rich composition effect on seismic properties (CO₂ solubility in
697 alkaline magmas can be as high as 15%, Brooker et al., 2001; Moussallam et al., 2015).
698 Nevertheless, the presence of 5 wt.% of water in 22% of peridotitic melt in the crystallized
699 peridotitic mantle strongly reduces the seismic velocities down to 39% for $V_{p_{\min}}$ and down to
700 33-34% for $V_{s_{1\min}}$ and $V_{s_{2\min}}$ (Table 3 and Figure 4). It should be noted that when fluid
701 inclusions are added in the crystallized peridotitic mantle, the S velocities decrease faster than
702 the P velocities, except from hydrous melt. This is due to the low bulk modulus used in the
703 computation which accounts for the supercritical behavior of water. This means that at the
704 depth/temperature conditions at which we modeled the xenoliths, water behaves as a gas,
705 leading to a faster decrease of V_p than V_s .

706 Numerous experimental and physical modeling (Clark and Lesher, 2017 and
707 references herein) demonstrate that the distribution of the melt in the peridotite may have a
708 strong influence on seismic velocity. In the case of computed fluid-filled inclusions in mantle
709 xenoliths, the fast velocities have orientations parallel or sub-parallel to the longest axes of
710 the inclusions (A1). This is observed for all inclusion orientations regardless of the fluid's
711 nature/composition (Figure 5). The maximum velocity is then obtained when the CPO of
712 olivine ([100] axis orientation) and maximum V_p and V_{s_2} are parallel to the longest axis of the
713 inclusion (parallel to A1) (Figure 4 and Figure 5).

714 For a peridotitic melt (anhydrous, 5% hydrous or with 2.5% CO₂), the lower bound
715 velocities values for lens-shape inclusions are lower and the V_{s_1} upper bound values are higher
716 than for acicular inclusions. Two patterns are competing: seismic components perpendicular
717 to the longest lens axes (perpendicular to A1 and A2) have to bypass the inclusion, whereas
718 seismic components parallel to the longest axes are "guided" along the inclusion elongation
719 (Figure 5).

720 Metasomatism can be viewed as present-day ascent of volatile-rich small-fraction
721 melts or past crystallized veins. The superposition of both veins would have a strong effect on
722 seismic velocities. However, if we assume that crystallized veins with clinopyroxene-
723 amphibole-phlogopite have a composition close to a peridotitic melt with water, the presence
724 of melt would further reduce velocities compared to crystallized veins. For peridotite with 6%
725 of lens-shaped inclusions filled with peridotitic melt with 5% H₂O, V_p decreases by 4 to 9% and
726 V_s decreases by 1 to 7% compared to peridotite with crystallized veins (PH18). For peridotite
727 with 22% lens-shaped inclusions filled with peridotitic melt with 5% H₂O (PH9), V_p decreases
728 by 9 to 31% and V_s decreases by 7 to 28% (Figure 4 vs Figure 5).

729

730 **6.4 In situ seismic properties versus travel-time tomography**

731 The scale over which petrophysics and seismic tomography consider the seismic wave
732 propagation varies from tens of centimeters up to several hundreds of kilometers,
733 respectively. At the kilometer-scale, the travel-time tomography reflects a current regional
734 and integrative effect of temperature, composition and anisotropy, whereas the seismic
735 properties calculations on xenoliths only refer to local properties for a given composition at a
736 specific depth (2 GPa in this study).

737 We propose here to use our in situ seismic property results to explain recent
 738 tomographic images in the NTD (Clutier et al., 2021). To transfer our natural sample-scale
 739 results to the regional scale, we first have to convert the mantle xenolith seismic variations
 740 into tomographic variations (Clutier et al., 2021). We compute the percentage difference
 741 between the IASP91 model (Kennett and Engdahl, 1991) and the mantle xenolith-estimated
 742 velocities as follows:

$$743 \quad \Delta V = \frac{V_x - V_i}{V_i} \times 100 \quad (3)$$

744 where V_x is the mantle xenoliths estimated V_p , and V_i is the velocity of IASP91 model (Kennett
 745 and Engdahl, 1991), also used as the reference in the P-wave tomography (Figure 7), at the
 746 mantle xenolith depth (40-90 km). The velocity variations relative to the IASP91 model (ΔV)
 747 are reported in Table 2 and Table 3. It should be noted that in relative arrival-time
 748 tomography, because the regional model is lost during the process, the 0% value of the final
 749 tomographic model may be different from the real global average (Bastow, 2012). In Clutier
 750 et al. (2021) tomographic inversion, the insertion of an a priori 3D crustal velocity model
 751 restricts this problem of shift between the regional mean model and the IASP91 mean model.
 752 Therefore, we can compare the velocity variations from the P-wave tomography and the ones
 753 from the xenoliths computed with equation (3). Moreover, to check this latter statement, we
 754 calculated the difference between the mean absolute velocity of the Clutier et al. (2021) in
 755 the resolved area, and the value of IASP91 at 80, 135 and 185 km depth. The Clutier et al.
 756 (2021) model has a maximum variation of -1.02% compared to IASP91 (-0.49% at 80km, -
 757 0.46% at 135km and -1.02% at 185km).

758 The travel-time tomography beneath the NTD shows that a low-velocity anomaly is
 759 present beneath the rift axis from the Moho (35 km) down to the asthenosphere (Figure 7 and
 760 Clutier et al., 2021). This central negative anomaly is flanked by two high-velocity anomalies,
 761 on the west side beneath the Tanzanian Craton and on the east side beneath the Proterozoic
 762 belt. The P velocity variations from tomography range from -15% to +9% for the whole area.
 763 It is restricted between -15% and -9% for the xenolith estimated location beneath Pello Hill
 764 (depth range from 40 to 90 km, Figure 7).

765 Such a range in V_p anomalies, also reported in density anomalies (Tiberi et al., 2019),
 766 cannot be accounted for by only a temperature effect. First, the depth of the partial melting
 767 estimated from Pello Hill melilitite is located at the downward border of the low-velocity
 768 tomographic anomaly at -2% of P velocity variation (Figure 7). Then, an increase of 100°C
 769 would decrease V_p by ca. 0.8% at 100 km and for a 1100-1200°C isotherm (Cammarano et al.,
 770 2003). The temperatures estimated from olivine-pyroxene equilibrium in mantle xenoliths
 771 suggest a temperature range isotherm of 1040 to 1200°C beneath the rift axis. These
 772 temperatures are then 300°C (80-90 km depth) and 600°C (40 km depth) higher than the
 773 plume-modified cratonic geotherm (Figure 6). Following this linear decrease of V_p with
 774 increasing temperature, such temperature variations can account for only 2.4% anomalies at
 775 80-90 km depth and 4.8% close to the Moho. Even if anelasticity may introduce non-linearity
 776 into temperature-seismic velocity relationship that are not taken into account here
 777 (Cammarano et al., 2003; Goes et al., 2000; Karato, 1993; Kuskov and Kronrod, 2006; Sobolev
 778 et al., 1996), the presence of metasomatic veins is probably the most robust candidate to
 779 explain velocity anomaly values of $\sim -10\%$ within the lithosphere.

780 To compare the seismic properties of crystallized vein-bearing peridotites and IASP91
 781 model, we calculate the effect of vein proportion on $V_{p_{\max}}$ and $V_{p_{\min}}$ for the vein bearing
 782 samples (PH4, PH9, PH18 and PH27), and correct the resulting velocities from temperature
 783 effects (1200°C instead of ambient temperature, Supplementary Material 3). We computed
 784 the velocities in three steps (see section 3.4.2) using the elastic properties of vein-free
 785 peridotite and the ones from veins from the xenoliths PH4, PH9, PH18 and PH27. The relative
 786 difference of the maximum and minimum V_p to IASP91 are plotted as a function of crystallized
 787 vein proportion in Figure 8.a. It also should be mentioned that for the calculated ΔV_p of
 788 peridotites with vein, $V_{p_{\max}}$ is slightly higher or equal to the IASP91 model ($\Delta V_{p_{\max}} = +0.6$ to
 789 $+4\%$, Figure 8.a) and $V_{p_{\min}}$ is lower than the IASP91 model ($\Delta V_{p_{\min}} = -5$; -9% , Figure 8.a). This
 790 difference is due to local anisotropy, which indicates higher temperatures and the percolation
 791 of a partial-melting front across the lithosphere.

792 The decrease of P velocity can be also explained by the presence of lens-shape fluid-
 793 filled inclusions (Figure 5 and Table 3). As with the crystallized veins, we calculated the vein
 794 proportion effect on the velocities for vein bearing samples at 2 GPa and 1200°C (Figure 8 .b
 795 to .d), but in two steps (see section 3.4.2), using the elastic properties of vein-free peridotite
 796 (at 2 GPa and 1200°C) and the ones from fluids (Table 4). Lens-shape hydrous melt would
 797 more efficiently reduce the P velocity in peridotite. The presence of 6 to 22% of lens-shape
 798 hydrous melt would decrease $V_{p_{\text{int}}}$ by 15 to 20% (Table 3 and Figure 8.b to .d, depending on
 799 inclusion orientation). Comparatively, for the same proportion of vein in the peridotite, $V_{p_{\text{int}}}$
 800 would decrease by 13 to 17% with lens-shape dry or 2.5%-CO₂ melt, and by 9 to 14% with lens-
 801 shape CaCO₃ melt (Figure 8.b to .d). Compared to crystallized veins, the mean velocity
 802 variations of fluid-filled inclusions are higher for hydrous, anhydrous and 2.5%- CO₂ melts,
 803 while they are similar for CaCO₃ melts.

804 Microstructures and CPO analysis of the Tanzanian xenoliths show that the
 805 lithospheric mantle in the Northern Tanzanian Divergence zone is pervasively deformed
 806 (Baptiste et al., 2015; Vauchez et al., 2005; this study). However, the strong heterogeneity in
 807 mantle xenoliths, microstructures, and olivine CPO suggest that this deformation was
 808 acquired during multiple tectonic events (Aulbach et al., 2011; Baptiste et al., 2015; Koornneef
 809 et al., 2009). Among peridotite from the rift axis, the most common olivine CPO pattern is the
 810 axial-[100] pattern, consistent with a strong simple shear component and a transtensional
 811 strain regime in the mantle lithosphere beneath the central part of the East-African rift
 812 (Baptiste et al., 2015; Tommasi et al., 1999). For these conditions, Vauchez et al. (2005) and
 813 Baptiste et al. (2015) suggest that the foliation is expected to be near vertical and the lineation
 814 close to horizontal and slightly oblique to the rift axis (Figure 9). Kendall et al. (2006) also
 815 suggested that vertical structures, such as vertical melt pockets oriented parallel to the rift
 816 axis, are also required in addition to olivine CPO to explain shear wave anisotropy for the more
 817 evolved northern part of the East African Rift System.

818 The maximum P velocity ($V_{p_{\max}}$) is representative of velocity parallel to the alignment
 819 of the olivine [100] axis, i.e., parallel to the foliation and perpendicular to the crystallized vein
 820 for peridotite with low vein proportions (PH18, Figure 4). However, the vein is oblique to the
 821 foliation and to the alignment of olivine [100] axis for high crystallized vein proportion (PH4,
 822 PH27). For lens-shaped fluid-filled melt inclusions, the maximum P velocity is parallel to the
 823 lens inclusion, while the minimum velocity is perpendicular to the maximum elongation of the
 824 inclusion.

825 Then, considering the incident tomographic P-wave being vertical, a vertical foliation
826 with horizontal lineation, and the presence of vertical metasomatic veins in the mantle
827 crosscutting obliquely or perpendicularly the foliation, we expect the global P wave path to
828 follow the mean P velocity ($V_{p_{int}}$) for crystallized veins and for fluid-filled veins of the modeled
829 mantle xenoliths velocities (Figure 8, and between models c) and d) in Figure 9). In other
830 words, the P velocity anomalies from tomography (-9 to -15% of V_p variation) could be
831 explained by high-temperature anomalies (200°C at 80-90 km) and the presence of 12 to 25%
832 of crystallized veins oblique to the vertical foliation, or between 8 and 15% of lens-shape fluid-
833 filled melt inclusions with a vertical orientation (Figure 9.d). Any hybrid composition between
834 these two end-members can also fulfill the conditions.

835 The lower bounds of our $V_{p_{min}}$ estimate (6-22% in Table 2, 6% in Table 3, and 6-15%
836 in Figure 8) are just above the mean vein proportion in the lithospheric mantle for MORB
837 source regions, around 2-5%, reported by Hirschmann and Stolper (1996). Our estimates
838 remain a mean/lower bound for vein proportion in NTD lithospheric mantle, as other
839 processes may favor higher values. The low Mg# in olivine in in-rift vein-bearing dunite
840 xenoliths (PH23, and Baptiste et al., 2015) might represent melt channels, or melt
841 accumulation levels within the mantle lithosphere, concentrating vein proportion in specific
842 areas (Berger, 1985; Berger and Vannier, 1984; Kelemen et al., 1995; Kelemen and Dick, 1995;
843 Tommasi et al., 2004). The presence of numerous and undeformed hydrous phases in veins or
844 diffuse pockets in mantle xenoliths suggests extensive post-kinematic metasomatism by
845 hydrous fluids or melts. The presence of deep asthenospheric alkaline magmas located at the
846 downward border of the low-velocity tomographic anomaly at -2% of P velocity variation and
847 close to the plume-modified geotherm (Figure 7 and Figure 6, respectively) may correspond
848 to the presence of deeply isolated melt pockets or interconnected melt (Clark and Leshar,
849 2017; Hammond and Humphreys, 2000). The presence of Archean metasomatic events from
850 ancient subduction zones and the presence of numerous volcanoes at the NTD may contribute
851 to a very high proportion of melt (Fritz et al., 2013; Koornneef et al., 2009; Mulibo and
852 Nyblade, 2013b; Pik et al., 2006; Tiberi et al., 2019). The maximum proportion of crystallized
853 and fluid-filled veins in metasomatic peridotites would, however, be less than 40% and 30%,
854 respectively (Figure 8) when considering $\Delta V_{p_{max}}$ for natural mineral assemblage in veins and
855 peridotitic melt (dry, hydrous and 2.5%-CO₂).

856 The petrological and petrophysical studies of xenolith samples provide constraints to
857 tomographic images in terms of composition and local structure of the mantle. The distinction
858 between the presence of crystallized melt and/or fluid could be further addressed with S-wave
859 lithospheric tomography below the NTD. The relative differences in both amplitude and
860 location of the V_p and V_s anomalies could give us relevant information to identify the presence
861 of melt/fluids and compositional variations (Ito et al., 1979; Watanabe, 1993). V_p is more
862 sensitive to the presence of gas, whereas V_s will drop faster when some melt is present. Then,
863 the tomographic V_p/V_s ratio would be essential to extract more information about the nature
864 of fluids (crystallized or melt-bearing veins) present in the magmatic area of the NTD (Husen
865 et al., 2004; Julian et al., 1998; Nakajima et al., 2001). Coupling the geochemical and
866 petrophysical study of xenolith samples and tomography can provide 3D information on
867 mantle dynamics, while paying attention to the change in spatial and temporal scale, since
868 tomography images the current state of the mantle.

869

870 **7 Conclusions**

871 We combined petrological and seismic property modeling of mantle xenoliths to
872 characterize the impact of metasomatic processes in the lithospheric mantle beneath the NTD
873 on the teleseismic P-wave tomography. First, the presence of an isotherm at 1040-1200°C
874 from olivine-pyroxene equilibria in peridotite beneath the NTD reveals temperature
875 anomalies up to 600°C compared to regional geotherm. This difference can explain 2.4 to 4.8%
876 of Vp decrease at lithospheric depth compared to global earth models. In addition, the seismic
877 properties of vein-bearing and vein-free mantle xenoliths sampled from the in-rift Pello Hill
878 volcano indicate a significant influence of vein proportion, orientation, and composition on
879 seismic properties.

880 When considering vertical foliation with azimuth parallel to the rift axis and
881 horizontal lineation, the presence of 12 to 25% of amphibole-phlogopite-clinopyroxene-
882 bearing crystallized veins can decrease of a vertically incident P-wave by 9 to 15% at 40-90 km
883 depth. The presence of active volcanoes beneath the rift argues for the presence of present-
884 day melt percolation. We estimate the partial melting for alkaline magmas to take place below
885 the LAB. The melt percolation (presence of fluid-filled veins) could explain the observed
886 tomographic low- velocity zone, which amplitudes are mainly controlled by the aspect ratio
887 of the inclusion and the nature of the fluid. 8 to 15% (depending on the melt composition) of
888 vertical lens-shape inclusions filled with melt would be necessary to decrease the tomographic
889 velocities by 9 to 15% at 40-90 km depth.

890

891 **8 Acknowledgments**

892 We would like to thank C. Nevado and D. Delmas, P. De Parseval and S. Gouy, F. Barou
893 for their valuable technical assistance in the thin section realization, microprobe analyses and
894 EBSD analyses. We thank S. A. Gibson and the anonymous reviewer for their thorough reviews,
895 which helped to improve the manuscript. We are also deeply grateful to Tanzanian institutions
896 that granted access to the field and participated to field work in the two mentioned projects
897 (NMAIST, Univ. Dodoma, Univ. Dar Es Salaam). Field work and research were under COSTECH
898 permits n° 2012-449-NA-2012-34 and 2017-284-NA-2017-269. This work was granted by
899 INSU-CNRS Tellus Rift project Hatari (chemical analyses), ANR-12-JS06-0004-01 CoLiBrEA
900 (sampling), INSU (Syster).

901

902

903 **Figure captions**

904

905 *Figure 1: Tecto-volcanic map of the NTD. The first-order geological units are indicated (Dawson*
906 *and Smith, 1988; Fritz et al., 2013; Smith and Mosley, 1993): orange for the Tanzanian Craton,*
907 *blue and green for the Western and Eastern parts, respectively, of the Mozambique Belt. The*

908 *inferred edges of the Masai block are represented by the blue dashed line. The major normal*
 909 *faults are represented by the continuous black lines: EBF = Eyasi Border Faults, NBF = Natron*
 910 *Border Fault, MBF = Manyara Border Fault, OOF = Ol Doinyo Ogol Fault, PBF = Pangani Border*
 911 *Fault. Green triangles indicate the location of the main volcanoes. The red star indicates the*
 912 *sample area of this study (Pello Hill). The ages of the volcanism are written in italic next to the*
 913 *volcanic edifices (Dawson, 1992; Macintyre et al., 1974; Mana et al., 2015, 2012; Manega,*
 914 *1993; Mollel, 2007; Nonnotte, 2007; Sherrod et al., 2013; Wilkinson et al., 1986). The two N-S*
 915 *and E-W chemical axes are represented by the green and purple arrows, respectively.*
 916 *Volcanoes abbreviations: B = Burko, El = Eledoi, Em = Embakai, Es = Essimngor, G = Gelai, H =*
 917 *Hanang, Ke = Kerimasi, Ket = Ketumbeine, Ki = Kilimanjaro, Kw = Kwahara, Lab = Labait, La =*
 918 *Lashaine, M = Monduli, Me = Meru, Ng = Ngorongoro, OL = Ol Doinyo Lengai, Olm = Olmani,*
 919 *PH = Pello Hill, T = Tarosero. The East-West red dashed line represents the track of the P-wave*
 920 *tomographic vertical cross-section in Figure 7.*

921 *Figure 2: Photomicrographs of Pello Hill mantle xenolith thin sections in plane polarized light:*
 922 *a) orthopyroxene, with amphibole inclusion, and reaction rim with clinopyroxene (PH13); b)*
 923 *interstitial clinopyroxene, orthopyroxene and chromite in PH18 dunite; c) Typical multi-*
 924 *millimeter amphibole/phlogopite/clinopyroxene patch surrounding chromites in PH13; d)*
 925 *amphibole-clinopyroxene aggregates around chromites in PH4 dunite; e) Diffused vein border*
 926 *with fine amphibole and clinopyroxene grains, and well-crystallized grains within the major*
 927 *vein in PH18; f) Distinct vein/peridotite boundary in PH4 dunite; g) Multi-millimeter phlogopite*
 928 *surrounded by aggregates of clinopyroxene-phlogopite-amphibole-olivine of 100-500 μm in*
 929 *the PH23 vein sample; h) Typical vein composition with clinopyroxene, amphibole, phlogopite,*
 930 *and ilmenite (PH9). Mineral abbreviations: Amph = amphibole; Chr = chromite; Cpx =*
 931 *clinopyroxene; Ilm = Ilmenite; Ol = olivine; Opx = orthopyroxene; Phl = phlogopite. Red*
 932 *continuous and dashed lines delimit the distinct and diffused vein/peridotite boundary,*
 933 *respectively.*

934 *Figure 3: Major element compositions for a) clinopyroxenes, b) and c) amphiboles, and d)*
 935 *phlogopites from the Pello Hill mantle xenoliths. Triangles are for in-vein minerals, circles for*
 936 *in-peridotite minerals and crosses for lava minerals. $\text{Mg\#} = \text{Mg}/(\text{Mg}+\text{Fe}^{2+})\times 100$.*

937 *Figure 4: Comparison between the whole sample, the peridotite (without vein), and the vein*
 938 *seismic properties (each one being computed in one step) for PH18, PH9, PH4, and PH27*
 939 *xenoliths, at pressure 2 GPa and 1200°C. The peridotite was computed directly with*
 940 *AnisEulerSC while the peridotite + vein and the vein were corrected from the temperature*
 941 *effect by applying a percentage decrease (Supplementary Material 3). The proportion of the*
 942 *vein in a sample is provided in brackets next to the sample name. All plots are lower*
 943 *hemisphere. Vein orientations are represented by the red lines on the olivine [100] axis pole*
 944 *figures. The black dashed lines on the V_p plot represent the elongation azimuth of sub-grains*
 945 *(undulose extinction) in the peridotite. N is the number of measurements used to compute the*
 946 *J-index (J) for the olivine.*

947 *Figure 5: Seismic property calculations with different lens-shape inclusion orientations and*
 948 *fluid filling in PH9 22% vein-bearing xenolith sample. Calculations are at pressure 2 GPa and*
 949 *temperature 1200°C with AnisEulerSC. The first row shows, a sketch of the orientation of the*
 950 *inclusions in the sample reference frame, where (X,Y) is the foliation plane and X the lineation*
 951 *(olivine [100] axis). A1 and A3 are the longest and shortest ellipse axes, respectively. $A1 = A2$*

952 = 5 and $A3 = 1$. AZ stands for the azimuth (counter clockwise) of the ellipse axes and INC for
 953 their vertical inclination. The velocity plots are lower hemisphere, and the maximum and
 954 minimum velocities are marked by a black square and a white circle, respectively.

955 *Figure 6: Calculated temperature and pressure for Pello Hill xenoliths with Brey and Köhler*
 956 *(1990) and Köhler and Brey (1990) thermobarometers (orthopyroxene-clinopyroxene and*
 957 *olivine-clinopyroxene couples). Lashaine P-T conditions are from Rudnick et al. (1994) and*
 958 *Gibson et al. (2013). The Labait xenoliths P-T conditions are from Lee and Rudnick (1999) and*
 959 *Koornneef et al. (2009). The P-T conditions of the partial melting of the Labait nephelinite are*
 960 *calculated from Baudouin and Parat (2020). Additional data of vein-free xenoliths from Pello*
 961 *Hill (black crosses, Dawson and Smith, 1988) were used to calculate P-T conditions as a*
 962 *comparison. The Pello Hill and Labait Moho were determined with receiver functions from*
 963 *Plasman et al. (2017) and A. Clutier personal communication, respectively. The LAB depth*
 964 *below the Labait and Pello Hill were estimated by Craig et al. (2011) with surface wave*
 965 *tomography (vertical resolution of ± 25 km). Cratonic geotherm (44 mW.m^{-2} , Selway et al.,*
 966 *2014), plume modified geotherm (50 mW.m^{-2} , Gibson and McKenzie, 2023), Proterozoic and*
 967 *Cenozoic geotherms (Artemieva, 2009) are also reported. The two peridotite solidi and the*
 968 *modeled melt CO_2 isopleths (thin grey lines, with CO_2 wt.% in the melt) are from Dasgupta et*
 969 *al. (2013).*

970 *Figure 7: West-East vertical cross-section at latitude 2.76°S (cross-section track on Figure 1) in*
 971 *the P-wave tomographic model from Clutier et al. (2021), with the depth of Pello Hill mantle*
 972 *xenoliths (grey triangles and diamonds) and lava partial melting (white star) from this study.*
 973 *Contours of velocity variations are every 3%. The LAB is taken from Craig et al. (2011) (vertical*
 974 *resolution of ± 25 km). Abbreviations: Kit. = Kitumbeine volcano; NBF = Natron Border Fault;*
 975 *OL = Ol Doinyo Lengai; OOF = Ol Doinyo Ogol Fault; PH = Pello Hill volcano.*

976 *Figure 8: Maximum (square), minimum (triangle) and mean (crosses) P-wave velocity*
 977 *variations (ΔV_p) computed for a) the crystallized vein-bearing mantle xenoliths with equation*
 978 *(3) and with temperature correction (1200°C), and b-d) for lens-shaped fluid-filled inclusions*
 979 *in PH9 mantle xenoliths: b) vertical veins perpendicular to the foliation (1:5:5), c) vertical veins*
 980 *parallel to the foliation (5:5:1), d) horizontal veins perpendicular to the foliation (5:1:5). The*
 981 *red and orange straight lines delimit the range of the tomographic low velocity variations*
 982 *induced by the metasomatizing fluid circulation. In graph a), the variation of velocity between*
 983 *the different samples for a common vein percentage is induced by the mineralogical*
 984 *assemblage.*

985 *Figure 9: Simplified structural diagram of a west-east profile in the North Tanzanian*
 986 *Divergence with representations (a-d) of possible relationship between fluid-filled veins (yellow*
 987 *planes) and the peridotites from natural xenoliths in the mantle. The orientation of the seismic*
 988 *velocities in the NTD are constrained by the vertical foliation and horizontal lineation in*
 989 *peridotite (with no veins) far from the rift axis (a), and by foliation, horizontal lineation and*
 990 *veins (perpendicular to the rift) in the rift axis (d), i.e. with intermediate vertical velocity. Spinel-*
 991 *garnet boundary is from Lee et al. (2000). Diagram modified from Kendall et al. (2006).*

992

993 **Tables**

994

995 *Table 1: Modal composition of Pello Hill mantle xenoliths determined by EBSD.*

Sample	Vein proportion in sample (%)	Total sample modal composition (%)						Vein composition (%)			
		Ol	Opx	Cpx	Phl	Amph	Ox	Cpx	Phl	Amph	
PH2	Harzburgite	0	77	21	0	0	1	0			
PH8	Dunite	0	84	0	7	0	7	0			
PH13	Harzburgite	0	85	13	0	0	1	1			
PH24	Harzburgite	0	85	13	1	0	1	0			
PH26	Dunite	0	92	4	2	1	0	0			
PH18	Dunite	6	85	6	5	2	2	0	45	37	18
PH9	Dunite	22	71	2	8	5	12	2	21	19	60

PH4	Dunite	62	33	0	40	19	8	0	59	29	12
PH27	Harzburgite	80	27	2	16	20	33	3	23	27	50
PH23	Vein	100	16	0	17	20	46	0			

996

997

Journal Pre-proofs

998 *Table 2: Seismic properties computed with AnisEulerSC at 2 GPa and 1200°C. Velocity variations are relative to the IAPS91 Earth model (Kennett*
 999 *and Engdahl, 1991) for Pello Hill mantle xenolith samples, crystallized full aggregates.*

Sam ple	Vein propo rtion in sampl e (%)	Seismic properties - AnisEuler													Variations relative to IAPS91	
		Vp max	Vp min	A V p	Vs1 max	Vs1 min	AV s1	Vs2 max	Vs2 min	AV s2	Vp/Vs 1 max	Vp/Vs 1 min	Vp/Vs 2 max	Vp/Vs 2 min	ΔVp max (%)	ΔVp min (%)
PH2	0	8.4	7.5	11 .3	4.6	4.4	4. 1	4.4	4.2	4. 8	1.9	1.7	1.9	1.8	4	-7
PH8	0	7.7	6.9	10 .9	4.3	4.1	4. 3	4.1	4.0	4. 0	1.8	1.7	1.9	1.7	-4	-14
PH1 3	0	8.5	7.5	13 .3	4.6	4.4	4. 3	4.4	4.2	6. 0	1.9	1.7	1.9	1.8	6	-7
PH2 4	0	8.4	7.5	11 .6	4.6	4.4	4. 5	4.4	4.2	5. 4	1.9	1.7	1.9	1.8	5	-7
PH2 6	0	8.4	7.3	14 .3	4.5	4.3	4. 2	4.3	4.1	6. 6	1.9	1.7	1.9	1.8	4	-10

PH1 8	6	8.2	7.1	14 .3	4.4	4.3	4. 4	4.3	4.0	6. 2	1.9	1.7	1.9	1.8	2	-11
PH9	22	7.6	6.5	15 .3	4.1	4.0	2. 7	4.0	3.7	6. 9	1.9	1.6	1.9	1.7	-6	-19
PH4	62	6.0	4.5	27 .9	3.4	3.1	10 .5	3.1	2.9	7. 4	1.8	1.4	1.9	1.5	-26	-44
PH2 7	80	5.4	4.6	16 .4	3.2	3.0	4. 9	3.0	2.9	3. 0	1.7	1.5	1.8	1.6	-32	-43
PH2 3	100	4.9	3.7	28 .2	2.8	2.6	7. 8	2.6	2.5	6. 3	1.8	1.4	1.9	1.5	-39	-54

1000

1001

1002
1003

Table 3: Seismic properties computed with AnisEulerSC at 2 GPa and 1200°C. Velocity variations are relative to the IAPS91 Earth model (Kennett and Engdahl, 1991) for Pello Hill mantle xenolith samples with vertical 5:5:1 fluid-filled inclusions.

Sample	Proportion of vein in sample (%)	Fluid/melt	Seismic properties with fluid or melt-filled veins - AnisEuler														Variations relative to IAPS91	
			Vp max	Vp min	A Vp	Vs ₁ max	Vs ₁ min	A Vs ₁	Vs ₂ max	Vs ₂ min	A Vs ₂	AVs max	Vp/Vs ₁ max	Vp/Vs ₁ min	Vp/Vs ₂ max	Vp/Vs ₂ min	ΔVp max (%)	ΔVp min (%)
PH18	6	Dry peridotitic melt	8.0	6.8	15.8	4.3	4.0	8.4	4.1	3.8	8.7	12.5	1.9	1.7	2.0	1.8	-1	-16
PH9	22		7.1	5.4	28.2	3.8	2.9	26.8	3.3	2.7	18.3	30.7	1.9	1.7	2.5	1.8	-11	-33
PH18	6	CaCO ₃ melt	8.1	7.0	13.8	4.4	4.0	8.3	4.1	3.8	9.2	12.4	1.9	1.7	2.0	1.8	0	-13
PH9	22		7.2	5.2	31.6	3.9	3.0	27.1	3.3	2.8	17.5	31.0	1.9	1.7	2.4	1.8	-11	-35

PH1 8	6	Peridotitic melt + 2.5% CO ₂	8.0	6.8	16.0	4.3	4.0	8.4	4.1	3.8	8.7	12.5	1.9	1.7	2.0	1.8	-1	-16
PH9	22		7.2	5.4	28.9	3.8	2.9	26.9	3.3	2.8	18.2	30.7	1.9	1.7	2.5	1.8	-11	-33

PH1 8	6	Peridotitic melt + 5% H ₂ O	7.9	6.5	19.7	4.3	4.0	8.6	4.1	3.8	7.9	12.6	1.9	1.6	2.0	1.7	-2	-20
PH9	22		6.9	4.5	42.3	3.8	2.9	28.2	3.1	2.7	14.2	32.1	1.9	1.6	2.4	1.6	-14	-44

1004

1005

1006 *Table 4: Bulk moduli used for the computation of velocities for the fluid-filled vein-bearing*
1007 *samples in Figure 5, at 1-4 GPa.*

Fluid	Bulk modulus (GPa)	Density (g/cm³)	Reference
Dry peridotitic melt	24	2.935	Sakamaki <i>et al.</i> 2010
CaCO ₃ melt	18.87	2.35	Genge <i>et al.</i> 1995
Peridotite melt + 5% H ₂ O	8.8	2.75	Sakamaki <i>et al.</i> 2009
Peridotite melt + 2.5% CO ₂	22.9	2.7	Sakamaki <i>et al.</i> 2011

1008

1009

1010 **References**

1011

1012 Abramson, E.H., Brown, J.M., Slutsky, L.J., Zaug, J., 1997. The elastic constants of San Carlos
1013 olivine to 17 GPa. *J. Geophys. Res. Solid Earth* 102, 12253–12263.
1014 <https://doi.org/10.1029/97jb00682>

1015 Adam, J., 1990. The Geochemistry and Experimental Petrology of Sodic Alkaline Basalts from
1016 Oatlands, Tasmania. *J. Petrol.* 31, 1201–1223.

1017 Adams, A., Nyblade, A., Weeraratne, D., 2012. Upper mantle shear wave velocity structure
1018 beneath the East African plateau: Evidence for a deep, plateau wide low velocity
1019 anomaly. *Geophys. J. Int.* 189, 123–142. [https://doi.org/10.1111/j.1365-
1020 246X.2012.05373.x](https://doi.org/10.1111/j.1365-246X.2012.05373.x)

1021 Albarède, F., 1992. How deep do common basaltic magmas form and differentiate? *J.*
1022 *Geophys. Res.* 97. <https://doi.org/10.1029/91jb02927>

1023 Albaric, J., Déverchère, J., Petit, C., Perrot, J., Le Gall, B., 2009. Crustal rheology and depth
1024 distribution of earthquakes: Insights from the central and southern East African Rift
1025 System. *Tectonophysics* 468, 28–41. <https://doi.org/10.1016/j.tecto.2008.05.021>

1026 Allen, R.M., Nolet, G., Morgan, W.J., Vogfjörd, K., Bergsson, B.H., Erlendsson, P., Foulger, G.R.,
1027 Jakobsdóttir, S., Julian, B.R., Pritchard, M., Ragnarsson, S., Stefánsson, R., 2002. Imaging
1028 the mantle beneath Iceland using integrated seismological techniques. *J. Geophys. Res.*
1029 *Solid Earth* 107, ESE 3-1-ESE 3-16. <https://doi.org/10.1029/2001jb000595>

1030 Almqvist, B.S.G., Mainprice, D., 2017. Seismic properties and anisotropy of the continental
1031 crust: Predictions based on mineral texture and rock microstructure. *Rev. Geophys.* 55,
1032 367–433. <https://doi.org/10.1002/2016RG000552>

1033 Artemieva, I.M., 2009. The continental lithosphere: Reconciling thermal, seismic, and
1034 petrologic data. *Lithos* 109, 23–46. <https://doi.org/10.1016/j.lithos.2008.09.015>

1035 Aulbach, S., Rudnick, R.L., McDonough, W.F., 2011. Evolution of the lithospheric mantle
1036 beneath the East African Rift in Tanzania and its potential signatures in rift magmas. *Geol.*
1037 *Soc. America* 2478, 105–125. [https://doi.org/10.1130/2011.2478\(06\)](https://doi.org/10.1130/2011.2478(06))

1038 Baker, J., Chazot, G., Menzies, M., Thirlwall, M., 1998. Metasomatism of the shallow mantle
1039 beneath Yemen by the Afar plume - implications for mantle plumes, flood volcanism, and
1040 intraplate volcanism. *Geology* 26, 431–434. [https://doi.org/10.1130/0091-
1041 7613\(1998\)026<0431:MOTSMB>2.3.CO;2](https://doi.org/10.1130/0091-7613(1998)026<0431:MOTSMB>2.3.CO;2)

1042 Baptiste, V., Tommasi, A., Vauchez, A., Demouchy, S., Rudnick, R., 2015. Deformation,
1043 hydration, and anisotropy of the lithospheric mantle in an active rift: Constraints from
1044 mantle xenoliths from the North Tanzanian Divergence of the East African Rift.
1045 *Tectonophysics* 639, 34–55. <https://doi.org/10.1016/j.tecto.2014.11.011>

- 1046 Bastow, I.D., 2012. Relative arrival-time upper-mantle tomography and the elusive
1047 background mean. *Geophys. J. Int.* 190, 1271–1278. <https://doi.org/10.1111/j.1365->
1048 246X.2012.05559.x
- 1049 Baudouin, C., Parat, F., 2020. Phlogopite-Olivine Nephelinites Erupted During Early Stage
1050 Rifting, North Tanzanian Divergence. *Front. Earth Sci.* 8, 1–22.
1051 <https://doi.org/10.3389/feart.2020.00277>
- 1052 Baudouin, C., Parat, F., Denis, C.M.M., Mangasini, F., 2016. Nephelinite lavas at early stage of
1053 rift initiation (Hanang volcano, North Tanzanian Divergence). *Contrib. to Mineral. Petrol.*
1054 171, 1–20. <https://doi.org/10.1007/s00410-016-1273-5>
- 1055 Baudouin, C., Parat, F., Michel, T., 2018. CO₂-rich phonolitic melt and carbonatite immiscibility
1056 in early stage of rifting: Melt inclusions from Hanang volcano (Tanzania). *J. Volcanol.*
1057 *Geotherm. Res.* 358, 261–272. <https://doi.org/10.1016/j.jvolgeores.2018.05.019>
- 1058 Bell, K., Simonetti, A., 1996. Carbonatite magmatism and plume activity: Implications from the
1059 Nd, Pb and Sr isotope systematics of oldoinyo lengai. *J. Petrol.* 37, 1321–1339.
1060 <https://doi.org/10.1093/petrology/37.6.1321>
- 1061 Berger, E.T., 1985. Hétérogénéité pétrographiques du manteau sud-pacifique, sous l'archipel
1062 des Australes : mise en évidence des enclaves ultramafiques. *Bull. Société géologique Fr.*
1063 1, 207–216.
- 1064 Berger, E.T., Vannier, M., 1984. Les dunites en enclaves dans les basaltes alcalins des îles
1065 océaniques: approche pétrologique. *Bull. Mineral.* 107, 649–663.
1066 <https://doi.org/10.3406/bulmi.1984.7809>
- 1067 Berryman, J.G., Berge, P.A., 1993. Rock elastic properties: dependence on microstructure.
- 1068 Bodinier, J.L., Vasseur, G., Vernières, J., Dupuy, C., Fabries, J., 1990. Mechanisms of mantle
1069 metasomatism: Geochemical evidence from the Iherz orogenic peridotite. *J. Petrol.* 31,
1070 597–628. <https://doi.org/10.1093/petrology/31.3.597>
- 1071 Braunger, S., Marks, M.A.W., Wenzel, T., Zaitsev, A.N., Markl, G., 2021. The Petrology of the
1072 Tarosero Volcanic Complex: Constraints on the Formation of Extrusive Agpaitic Rocks. *J.*
1073 *Petrol.* 62, 1–34. <https://doi.org/10.1093/petrology/egab015>
- 1074 Brey, G.P., Köhler, T., 1990. Geothermobarometry in four-phase Iherzolites II. New
1075 thermobarometers, and practical assessment of existing thermobarometers. *J. Petrol.*
1076 31, 1353–1378. <https://doi.org/10.1093/petrology/31.6.1353>
- 1077 Brooker, R.A., Kohn, S.C., Holloway, J.R., McMillan, P.F., 2001. Structural controls on the
1078 solubility of CO₂ in silicate melts part I: Bulk solubility data. *Chem. Geol.* 174, 225–239.
1079 [https://doi.org/10.1016/S0009-2541\(00\)00353-3](https://doi.org/10.1016/S0009-2541(00)00353-3)
- 1080 Burton, K.W., Schiano, P., Birck, J.L., Allègre, C.J., Rehkämper, M., Halliday, A.N., Dawson, J.B.,
1081 2000. The distribution and behaviour of rhenium and osmium amongst mantle minerals
1082 and the age of the lithospheric mantle beneath Tanzania. *Earth Planet. Sci. Lett.* 183, 93–

- 1083 106. [https://doi.org/10.1016/S0012-821X\(00\)00259-4](https://doi.org/10.1016/S0012-821X(00)00259-4)
- 1084 Cammarano, F., Goes, S., Vacher, P., Giardini, D., 2003. Inferring upper-mantle temperatures
1085 from seismic velocities. *Phys. Earth Planet. Inter.* 138, 197–222.
1086 [https://doi.org/10.1016/S0031-9201\(03\)00156-0](https://doi.org/10.1016/S0031-9201(03)00156-0)
- 1087 Chai, M., Brown, J.M., Slutsky, L.J., 1997. The elastic constants of an aluminous orthopyroxene
1088 12.5 GPa. *J. Geophys. Res.* 102, 779–785. <https://doi.org/10.1029/97JB00893>
- 1089 Chesley, J.T., Rudnick, R.L., Lee, C.T., 1999. Re-Os systematics of mantle xenoliths from the
1090 East African Rift: Age, structure, and history of the Tanzanian craton. *Geochim.*
1091 *Cosmochim. Acta* 63, 1203–1217. [https://doi.org/10.1016/S0016-7037\(99\)00004-6](https://doi.org/10.1016/S0016-7037(99)00004-6)
- 1092 Chheda, T.D., Mookherjee, M., Mainprice, D., Dos Santos, A.M., Molaison, J.J., Chantel, J.,
1093 Manthilake, G., Bassett, W.A., 2014. Structure and elasticity of phlogopite under
1094 compression: Geophysical implications. *Phys. Earth Planet. Inter.* 233, 1–12.
1095 <https://doi.org/10.1016/j.pepi.2014.05.004>
- 1096 Christoffel, E.B., 1877. Ueber die Fortpflanzung von Stößen durch elastische feste Körper.
1097 *Ann. di Mat. Pura ed Appl.* 8, 193–243. <https://doi.org/10.1007/BF02420789>
- 1098 Clark, A.N., Leshner, C.E., 2017. Elastic properties of silicate melts: Implications for low velocity
1099 zones at the lithosphere-asthenosphere boundary. *Sci. Adv.* 3, 1–5.
1100 <https://doi.org/10.1126/sciadv.1701312>
- 1101 Clutier, A., Gautier, S., Tiberi, C., 2021. Hybrid local and teleseismic P-wave tomography in
1102 North Tanzania: Role of inherited structures and magmatism on continental rifting.
1103 *Geophys. J. Int.* 224, 1588–1606. <https://doi.org/10.1093/gji/ggaa538>
- 1104 Cohen, R.S., O’Nions, R.K., Dawson, J.B., 1984. Isotope geochemistry of xenoliths from East
1105 Africa: Implications for development of mantle reservoirs and their interaction. *Earth*
1106 *Planet. Sci. Lett.* 68, 209–220. [https://doi.org/10.1016/0012-821X\(84\)90153-5](https://doi.org/10.1016/0012-821X(84)90153-5)
- 1107 Condamine, P., Médard, E., Devidal, J.L., 2016. Experimental melting of phlogopite-peridotite
1108 in the garnet stability field. *Contrib. to Mineral. Petrol.* 171.
1109 <https://doi.org/10.1007/s00410-016-1306-0>
- 1110 Corti, G., Iandelli, I., Cerca, M., 2013. Experimental modeling of rifting at craton margins.
1111 *Geosphere* 9, 138–154. <https://doi.org/10.1130/GES00863.1>
- 1112 Courtillot, V., Jaupart, C., Manighetti, I., Tapponnier, P., Besse, J., 1999. On causal links
1113 between flood basalts and continental breakup. *Earth Planet. Sci. Lett.* 166, 177–195.
1114 [https://doi.org/10.1016/S0012-821X\(98\)00282-9](https://doi.org/10.1016/S0012-821X(98)00282-9)
- 1115 Courtillot, V.E., Renne, P.R., 2003. On the ages of flood basalt events. *Comptes Rendus -*
1116 *Geosci.* 335, 113–140. [https://doi.org/10.1016/S1631-0713\(03\)00006-3](https://doi.org/10.1016/S1631-0713(03)00006-3)
- 1117 Craig, T.J., Jackson, J.A., Priestley, K., Mckenzie, D., 2011. Earthquake distribution patterns in
1118 Africa: Their relationship to variations in lithospheric and geological structure, and their
1119 rheological implications. *Geophys. J. Int.* 185, 403–434. <https://doi.org/10.1111/j.1365->

- 1120 246X.2011.04950.x
- 1121 Da Silva, C.R.S., Karki, B.B., Stixrude, L., Wentzcovitch, R.M., 1999. Ab initio study of the elastic
1122 behavior of MgSiO₃ ilmenite at high pressure. *Geophys. Res. Lett.* 26, 943–946.
1123 <https://doi.org/10.1029/1999GL900149>
- 1124 Dasgupta, R., Mallik, A., Tsuno, K., Withers, A.C., Hirth, G., Hirschmann, M.M., 2013. Carbon-
1125 dioxide-rich silicate melt in the Earth's upper mantle. *Nature* 493, 211–215.
1126 <https://doi.org/10.1038/nature11731>
- 1127 Dawson, J.B., 2012. Nephelinite-melilitite-carbonatite relationships: Evidence from
1128 Pleistocene-recent volcanism in northern Tanzania. *Lithos* 152, 3–10.
1129 <https://doi.org/10.1016/j.lithos.2012.01.008>
- 1130 Dawson, J.B., 2008. The Gregory Rift Valley and Neogene-Recent Volcanoes of Northern
1131 Tanzania.
- 1132 Dawson, J.B., 1997. Neogene–Recent rifting and volcanism in northern Tanzania: relevance
1133 for comparisons between the Gardar province and the East African Rift valley. *Mineral.*
1134 *Mag.* 61, 543–548. <https://doi.org/10.1180/minmag.1997.061.407.06>
- 1135 Dawson, J.B., 1992. Neogene tectonics and volcanicity in the North Tanzania sector of the
1136 Gregory Rift Valley: contrasts with the Kenya sector. *Tectonophysics* 204.
1137 [https://doi.org/10.1016/0040-1951\(92\)90271-7](https://doi.org/10.1016/0040-1951(92)90271-7)
- 1138 Dawson, J.B., 1984. Contrasting types of upper-mantle metasomatism? *Dev. Petrol.* 11, 289–
1139 294. <https://doi.org/10.1016/B978-0-444-42273-6.50028-6>
- 1140 Dawson, J.B., Smith, J. V., 1988. Metasomatized and veined upper-mantle xenoliths from Pello
1141 Hill, Tanzania: evidence for anomalously-light mantle beneath the Tanzanian sector of
1142 the East African Rift Valley. *Contrib. to Mineral. Petrol.* 100, 510–527.
1143 <https://doi.org/10.1007/BF00371380>
- 1144 De Moor, J.M., Fischer, T.P., King, P.L., Botcharnikov, R.E., Hervig, R.L., Hilton, D.R., Barry, P.H.,
1145 Mangasini, F., Ramirez, C., 2013. Volatile-rich silicate melts from Oldoinyo Lengai volcano
1146 (Tanzania): Implications for carbonatite genesis and eruptive behavior. *Earth Planet. Sci.*
1147 *Lett.* 361, 379–390. <https://doi.org/10.1016/j.epsl.2012.11.006>
- 1148 Delpech, G., Grégoire, M., O'Reilly, S.Y., Cottin, J.Y., Moine, B., Michon, G., Giret, A., 2004.
1149 Feldspar from carbonate-rich silicate metasomatism in the shallow oceanic mantle under
1150 Kerguelen Islands (South Indian Ocean). *Lithos* 75, 209–237.
1151 <https://doi.org/10.1016/j.lithos.2003.12.018>
- 1152 Deschamps, F., Trampert, J., 2003. Mantle tomography and its relation to temperature and
1153 composition. *Phys. Earth Planet. Inter.* 140, 277–291.
1154 <https://doi.org/10.1016/j.pepi.2003.09.004>
- 1155 Dixon, J., Clague, D.A., Cousens, B., Monsalve, M.L., Uhl, J., 2008. Carbonatite and silicate melt
1156 metasomatism of the mantle surrounding the Hawaiian plume: Evidence from volatiles,

- 1157 trace elements, and radiogenic isotopes in rejuvenated-stage lavas from Niihau, Hawaii.
1158 Geochemistry, Geophys. Geosystems 9. <https://doi.org/10.1029/2008GC002076>
- 1159 Ebinger, C., Djomani, Y.P., Mbede, E., Foster, A., Dawson, J.B., 1997. Rifting Archaean
1160 lithosphere: The Eyasi-Manyara-Natron rifts, East Africa. *J. Geol. Soc. London.* 154, 947–
1161 960. <https://doi.org/10.1144/gsjgs.154.6.0947>
- 1162 Ebinger, C.J., Sleep, N.H., 1998. Cenozoic magmatism throughout east Africa resulting from
1163 impact of a single plume. *Nature* 395, 788–791.
- 1164 Ebinger, C.J., Yemane, T., Harding, D.J., Tesfaye, S., Kelley, S., Rex, D.C., 2000. Rift deflection,
1165 migration, and propagation: Linkage of the Ethiopian and Eastern rifts, Africa. *Bull. Geol.*
1166 *Soc. Am.* 112, 163–176. [https://doi.org/10.1130/0016-](https://doi.org/10.1130/0016-7606(2000)112<163:RDMAPL>2.0.CO;2)
1167 [7606\(2000\)112<163:RDMAPL>2.0.CO;2](https://doi.org/10.1130/0016-7606(2000)112<163:RDMAPL>2.0.CO;2)
- 1168 Eshelby, J.D., 1957. The determination of the elastic field of an ellipsoidal inclusion, and
1169 related problems. *Proc. R. Soc. London. Ser. A. Math. Phys. Sci.* 241, 376–396.
1170 <https://doi.org/https://doi.org/10.1098/rspa.1957.0133>
- 1171 Faul, U.H., Jackson, I., 2005. The seismological signature of temperature and grain size
1172 variations in the upper mantle. *Earth Planet. Sci. Lett.* 234, 119–134.
1173 <https://doi.org/10.1016/j.epsl.2005.02.008>
- 1174 Fishwick, S., 2010. Surface wave tomography: Imaging of the lithosphere-asthenosphere
1175 boundary beneath central and southern Africa? *Lithos* 120, 63–73.
1176 <https://doi.org/10.1016/j.lithos.2010.05.011>
- 1177 Foley, S.F., Link, K., Tiberindwa, J. V., Barifajjo, E., 2012. Patterns and origin of igneous activity
1178 around the Tanzanian craton. *J. African Earth Sci.* 62, 1–18.
1179 <https://doi.org/10.1016/j.jafrearsci.2011.10.001>
- 1180 Foster, A., Ebinger, C., Mbede, E., Rex, D., 1997. Tectonic development of the northern
1181 Tanzanian sector of the East African Rift System. *J. Geol. Soc. London.* 154, 689–700.
1182 <https://doi.org/10.1144/gsjgs.154.4.0689>
- 1183 Frey, F.A., Green, D.H., Roy, S.D., 1978. Integrated Models of Basalt Petrogenesis : A Study of
1184 Quartz Tholeiites to Olivine Melilitites from South Eastern Australia Utilizing Geochemical
1185 and Experimental Petrological Data. *J. Petrol.* 19, 463–513.
- 1186 Fritz, H., Abdelsalam, M., Ali, K.A., Bingen, B., Collins, A.S., Fowler, A.R., Ghebreab, W.,
1187 Hauzenberger, C.A., Johnson, P.R., Kusky, T.M., Macey, P., Muhongo, S., Stern, R.J., Viola,
1188 G., 2013. Orogen styles in the East African Orogen: A review of the Neoproterozoic to
1189 Cambrian tectonic evolution. *J. African Earth Sci.* 86, 65–106.
1190 <https://doi.org/10.1016/j.jafrearsci.2013.06.004>
- 1191 Genge, M.J., Price, G.D., Jones, A.P., 1995. Molecular dynamics simulations of CaCO₃ melts to
1192 mantle pressures and temperatures: implications for carbonatite magmas. *Earth Planet.*
1193 *Sci. Lett.* 131, 225–238. [https://doi.org/10.1016/0012-821X\(95\)00020-D](https://doi.org/10.1016/0012-821X(95)00020-D)

- 1194 George, R., Rogers, N., Kelley, S., 1998. Earliest magmatism in Ethiopia: Evidence for two
1195 mantle plumes in one flood basalt province. *Geology* 26, 923–926.
- 1196 Gibson, S.A., McKenzie, D., 2023. On the role of Earth’s lithospheric mantle in global volatile
1197 cycles. *Earth Planet. Sci. Lett.* 602, 117946. <https://doi.org/10.1016/j.epsl.2022.117946>
- 1198 Gibson, S.A., McMahon, S.C., Day, J.A., Dawson, J.B., 2013. Highly refractory lithospheric
1199 mantle beneath the Tanzanian craton: Evidence from Lashaine pre-metasomatic garnet-
1200 bearing peridotites. *J. Petrol.* 54, 1503–1546. <https://doi.org/10.1093/petrology/egt020>
- 1201 Goes, S., Govers, R., Vacher, P., 2000. Shallow mantle temperatures under Europe from P and
1202 S wave tomography. *J. Geophys. Res. Solid Earth* 105, 11153–11169.
1203 <https://doi.org/10.1029/1999jb900300>
- 1204 Green, D.H., Falloon, T.J., 1998. Pyrolite: A Ringwood Concept and Its Current Expression, in:
1205 The Earth’s Mantle: Composition, Structure, and Evolution. Cambridge University Press,
1206 Cambridge, pp. 311–378. <https://doi.org/10.1017/cbo9780511573101.010>
- 1207 Grégoire, M., Moine, B.N., O’Reilly, S.Y., Cottin, J.Y., Giret, A., 2000. Trace element residence
1208 and partitioning in mantle xenoliths metasomatized by highly alkaline, silicate- and
1209 carbonate-rich melts (Kerguelen Islands, Indian Ocean). *J. Petrol.* 41, 477–509.
1210 <https://doi.org/10.1093/petrology/41.4.477>
- 1211 Griffin, W.L., O’Reilly, S.Y., Afonso, J.C., Begg, G.C., 2009. The composition and evolution of
1212 lithospheric mantle: A re-evaluation and its tectonic implications. *J. Petrol.* 50, 1185–
1213 1204. <https://doi.org/10.1093/petrology/egn033>
- 1214 Grijalva, A., Nyblade, A.A., Homman, K., Accardo, N.J., Gaherty, J.B., Ebinger, C.J., Shillington,
1215 D.J., Chindandali, P.R.N., Mbogoni, G., Ferdinand, R.W., Mulibo, G., O’Donnell, J.P.,
1216 Kachingwe, M., Tepp, G., 2018. Seismic Evidence for Plume- and Craton-Influenced Upper
1217 Mantle Structure Beneath the Northern Malawi Rift and the Rungwe Volcanic Province,
1218 East Africa. *Geochemistry, Geophys. Geosystems* 19, 3980–3994.
1219 <https://doi.org/10.1029/2018GC007730>
- 1220 Guzmics, T., Mitchell, R.H., Szabó, C., Berkesi, M., Milke, R., Ratter, K., 2012. Liquid
1221 immiscibility between silicate, carbonate and sulfide melts in melt inclusions hosted in
1222 co-precipitated minerals from Kerimasi volcano (Tanzania): Evolution of carbonated
1223 nephelinitic magma. *Contrib. to Mineral. Petrol.* 164, 101–122.
1224 <https://doi.org/10.1007/s00410-012-0728-6>
- 1225 Hammond, J.O.S., Kendall, J.M., 2016. Constraints on melt distribution from seismology: A
1226 case study in Ethiopia. *Geol. Soc. Spec. Publ.* 420, 127–147.
1227 <https://doi.org/10.1144/SP420.14>
- 1228 Hammond, W.C., Humphreys, E.D., 2000. Upper mantle seismic wave attenuation: Effects of
1229 realistic partial melt distribution. *J. Geophys. Res. Solid Earth* 105, 10987–10999.
1230 <https://doi.org/10.1029/2000jb900042>
- 1231 Hielscher, R., Schaeben, H., 2008. A novel pole figure inversion method: Specification of the

- 1232 MTEX algorithm. *J. Appl. Crystallogr.* 41, 1024–1037.
1233 <https://doi.org/10.1107/S0021889808030112>
- 1234 Hill, R., 1965. A self-consistent mechanics of composite materials. *J. Mech. Phys. Solids* 13,
1235 213–222. [https://doi.org/10.1016/0022-5096\(65\)90010-4](https://doi.org/10.1016/0022-5096(65)90010-4)
- 1236 Hirschmann, M.M., Stolper, E.M., 1996. A possible role for garnet pyroxenite in the origin of
1237 the “garnet signature” in MORB. *Contrib. to Mineral. Petrol.* 124, 185–208.
1238 <https://doi.org/10.1007/s004100050184>
- 1239 Huerta, A.D., Nyblade, A.A., Reusch, A.M., 2009. Mantle transition zone structure beneath
1240 Kenya and Tanzania: More evidence for a deep-seated thermal upwelling in the mantle.
1241 *Geophys. J. Int.* 177, 1249–1255. <https://doi.org/10.1111/j.1365-246X.2009.04092.x>
- 1242 Hui, H., Peslier, A.H., Rudnick, R.L., Simonetti, A., Neal, C.R., 2015. Plume-cratonic lithosphere
1243 interaction recorded by water and other trace elements in peridotite xenoliths from the
1244 Labait volcano, Tanzania. *Geochemistry Geophys. Geosystems* 16, 1687–1710.
1245 <https://doi.org/10.1002/2014GC005684.Key>
- 1246 Husen, S., Smith, R.B., Waite, G.P., 2004. Evidence for gas and magmatic sources beneath the
1247 Yellowstone volcanic field from seismic tomographic imaging. *J. Volcanol. Geotherm. Res.*
1248 131, 397–410. [https://doi.org/10.1016/S0377-0273\(03\)00416-5](https://doi.org/10.1016/S0377-0273(03)00416-5)
- 1249 Ismail, W. Ben, Mainprice, D., 1998. An olivine fabric database: An overview of upper mantle
1250 fabrics and seismic anisotropy. *Tectonophysics* 296, 145–157.
1251 [https://doi.org/10.1016/S0040-1951\(98\)00141-3](https://doi.org/10.1016/S0040-1951(98)00141-3)
- 1252 Ito, H., Devilbiss, J., Nur, A., 1979. Compressional and shear waves in saturated rock during
1253 water-stream transition. *J. Geophys. Res.* 84, 4731–4735.
1254 <https://doi.org/10.1029/JB084iB09p04731>
- 1255 Julian, B.R., Pitt, A.M., Foulger, G.R., 1998. Seismic image of a CO₂ reservoir beneath a
1256 seismically active volcano. *Geophys. J. Int.* 133, F7–F10. <https://doi.org/10.1046/j.1365-246x.1998.1331540.x>
- 1258 Karato, S.I., 1993. Importance of anelasticity in the interpretation of seismic tomography.
1259 *Geophys. Res. Lett.* 20, 1623–1626.
- 1260 Karato, S.I., Jung, H., 1998. Water, partial melting and the origin of the seismic low velocity
1261 and high attenuation zone in the upper mantle. *Earth Planet. Sci. Lett.* 157, 193–207.
1262 [https://doi.org/10.1016/S0012-821X\(98\)00034-X](https://doi.org/10.1016/S0012-821X(98)00034-X)
- 1263 Kelemen, P.B., Dick, H.J.B., 1995. Focused melt flow and localized deformation in the upper
1264 mantle: juxtaposition of replacive dunite and ductile shear zones in the Josephine
1265 peridotite, SW Oregon. *J. Geophys. Res.* 100, 423–438.
1266 <https://doi.org/10.1029/94JB02063>
- 1267 Kelemen, P.B., Shimizu, N., Salters, V.J.M., 1995. Extraction of mid-ocean-ridge basalt from
1268 the upwelling mantle by focused flow of melt in dunite channels. *Nature* 375, 747–753.

- 1269 <https://doi.org/10.1038/375747a0>
- 1270 Kendall, J.M., 2000. Seismic anisotropy in the boundary layers of the mantle, in: Karato, S.,
1271 Forte, A., Liebermann, R., Masters, G., Stixrude, L. (Eds.), *Geophysical Monograph Series*.
1272 American Geophysical Union Washington, DC, pp. 133–159.
- 1273 Kendall, J.M., Pilidou, S., Keir, D., Bastow, I.D., Stuart, G.W., Ayele, A., 2006. Mantle upwellings,
1274 melt migration and the rifting of Africa: Insights from seismic anisotropy. *Geol. Soc. Spec.*
1275 *Publ.* 259, 55–72. <https://doi.org/10.1144/GSL.SP.2006.259.01.06>
- 1276 Kennett, B.L.N., Engdahl, E.R., 1991. Travel times for global earthquake location and phase
1277 association. *Geophys. J. Int.* 105, 429–465. <https://doi.org/10.17611/DP/9991809>
- 1278 Kim, E., Kim, Y.H., Mainprice, D., 2020. AnisEulerSC: A MATLAB program combined with MTEX
1279 for modeling the anisotropic seismic properties of a polycrystalline aggregate with
1280 microcracks using self-consistent approximation. *Comput. Geosci.* 145, 104589.
1281 <https://doi.org/10.1016/j.cageo.2020.104589>
- 1282 Klaudius, J., Keller, J., 2006. Peralkaline silicate lavas at Oldoinyo Lengai, Tanzania. *Lithos* 91,
1283 173–190. <https://doi.org/10.1016/j.lithos.2006.03.017>
- 1284 Klemme, S., 2004. The influence of Cr on the garnet-spinel transition in the Earth's mantle:
1285 Experiments in the system MgO-Cr₂O₃-SiO₂ and thermodynamic modelling. *Lithos* 77,
1286 639–646. <https://doi.org/10.1016/j.lithos.2004.03.017>
- 1287 Koch, N., Welzel, U., Wern, H., Mittemeijer, E.J., 2004. Mechanical elastic constants and
1288 diffraction stress factors of macroscopically elastically anisotropic polycrystals: The effect
1289 of grain-shape (morphological) texture. *Philos. Mag.* 84, 3547–3570.
1290 <https://doi.org/10.1080/14786430412331284504>
- 1291 Köhler, T.P., Brey, G.P., 1990. Calcium exchange between olivine and clinopyroxene calibrated
1292 as a geothermobarometer for natural peridotites from 2 to 60 kb with applications.
1293 *Geochim. Cosmochim. Acta* 54, 2375–2388. [https://doi.org/10.1016/0016-7037\(90\)90226-B](https://doi.org/10.1016/0016-7037(90)90226-B)
- 1295 Koornneef, J.M., Davies, G.R., Döpp, S.P., Vukmanovic, Z., Nikogosian, I.K., Mason, P.R.D.,
1296 2009. Nature and timing of multiple metasomatic events in the sub-cratonic lithosphere
1297 beneath Labait, Tanzania. *Lithos* 112, 896–912.
1298 <https://doi.org/10.1016/j.lithos.2009.04.039>
- 1299 Koptev, A., Burov, E., Calais, E., Leroy, S., Gerya, T., Guillou-Frottier, L., Cloetingh, S., 2016.
1300 Contrasted continental rifting via plume-craton interaction: Applications to Central East
1301 African Rift. *Geosci. Front.* 7, 221–236. <https://doi.org/10.1016/j.gsf.2015.11.002>
- 1302 Koptev, A., Burov, E., Gerya, T., Le Pourhiet, L., Leroy, S., Calais, E., Jolivet, L., 2018.
1303 Tectonophysics Plume-induced continental rifting and break-up in ultra-slow extension
1304 context: Insights from 3D numerical modeling. *Tectonophysics* 746, 121–137.
1305 <https://doi.org/10.1016/j.tecto.2017.03.025>

- 1306 Koptev, A., Calais, E., Burov, E., Leroy, S., Gerya, T., 2015. Dual continental rift systems
1307 generated by plume-lithosphere interaction. *Nat. Geosci.* 8, 388–392.
1308 <https://doi.org/10.1038/ngeo2401>
- 1309 Kuskov, O.L., Kronrod, V.A., 2006. Determining the temperature of the Earth's continental
1310 upper mantle from geochemical and seismic data. *Geochemistry Int.* 44, 232–248.
1311 <https://doi.org/10.1134/S0016702906030025>
- 1312 Le Gall, B., Nonnotte, P., Rolet, J., Benoit, M., Guillou, H., Mousseau-Nonnotte, M., Albaric, J.,
1313 Deverchère, J., 2008. Rift propagation at craton margin. Distribution of faulting and
1314 volcanism in the North Tanzanian Divergence (East Africa) during Neogene times.
1315 *Tectonophysics* 448, 1–19. <https://doi.org/10.1016/j.tecto.2007.11.005>
- 1316 Leake, B.E., Woolley, A.R., Arps, C.E.S., Birch, W.D., Gilbert, M.C., Grice, J.D., Hawthorne, F.C.,
1317 Kato, A., Kisch, H.J., Krivovichev, V.G., Linthout, K., Laird, J., Mandarino, J.A., Maresch, W.
1318 V., Nickel, E.H., Rock, N.M.S., Schumacher, J.C., Smith, D.C., Stephenson, N.C.N.,
1319 Ungaretti, L., Whittaker, E.J.W., Youzhi, G., 1997. Nomenclature of amphiboles: Report
1320 of the subcommittee on amphiboles of the international mineralogical association,
1321 commission on new minerals and mineral names. *Am. Mineral.* 82, 1019–1037.
1322 <https://doi.org/10.1180/minmag.1997.061.405.13>
- 1323 Lee, C.T.A., Rudnick, R.L., 1999. Compositionally stratified cratonic lithosphere: petrology and
1324 geochemistry of peridotite xenoliths from the Labait tuff cone volcano, Tanzania. *Proc.*
1325 *7th Internatl. Kimberl. Conf.* 503–521.
- 1326 Lee, H., Fischer, T.P., Muirhead, J.D., Ebinger, C.J., Kattenhorn, S.A., Sharp, Z.D., Kianji, G.,
1327 Takahata, N., Sano, Y., 2017. Incipient rifting accompanied by the release of
1328 subcontinental lithospheric mantle volatiles in the Magadi and Natron basin, East Africa.
1329 *J. Volcanol. Geotherm. Res.* 346, 118–133.
1330 <https://doi.org/10.1016/j.jvolgeores.2017.03.017>
- 1331 Lee, W.J., Huang, W.L., Wyllie, P., 2000. Melts in the mantle modeled in the system CaO-MgO-
1332 SiO₂-CO₂ at 2.7 GPa. *Contrib. to Mineral. Petrol.* 138, 199–213.
1333 <https://doi.org/10.1007/s004100050557>
- 1334 Lenardic, A., Moresi, L.-N., Mühlhaus, H., 2003. Longevity and stability of cratonic lithosphere:
1335 Insights from numerical simulations of coupled mantle convection and continental
1336 tectonics. *J. Geophys. Res. Solid Earth* 108, 1–15. <https://doi.org/10.1029/2002jb001859>
- 1337 Longhi, J., Fram, M.S., Vander Auwera, J., Montieth, J.N., 1993. Pressure effects, kinetics, and
1338 rheology of anorthositic and related magmas. *Am. Mineral.* 78, 1016–1030.
- 1339 MacDonald, R., Rogers, N.W., Fitton, J.G., Black, S., Smith, M., 2001. Plume-Lithosphere
1340 Interactions in the Generation of the Basalts of the Kenya Rift, East Africa. *J. Petrol.* 42,
1341 877–900. <https://doi.org/10.1093/petrology/42.5.877>
- 1342 Macintyre, R.M., Mitchell, J.G., Dawson, J.B., 1974. Age of fault movements in Tanzanian
1343 sector of East African Rift System. *Nature* 247, 354–356.

- 1344 Mainprice, D., 1997. Modelling the anisotropic seismic properties of partially molten rocks
1345 found at mid-ocean ridges. *Tectonophysics* 279, 161–179.
1346 [https://doi.org/10.1016/s0040-1951\(97\)00122-4](https://doi.org/10.1016/s0040-1951(97)00122-4)
- 1347 Mainprice, D., Bachmann, F., Hielscher, R., Schaeben, H., Lloyd, G.E., 2011. Calculating
1348 anisotropic piezoelectric properties from texture data using the MTEX open source
1349 package. *Geol. Soc. Spec. Publ.* 409, 223–249. <https://doi.org/10.1144/SP409.2>
- 1350 Mana, S., Furman, T., Carr, M.J., Mollel, G.F., Mortlock, R.A., Feigenson, M.D., Turrin, B.D.,
1351 Swisher, C.C., 2012. Geochronology and geochemistry of the Essimingor volcano: Melting
1352 of metasomatized lithospheric mantle beneath the North Tanzanian Divergence zone
1353 (East African Rift). *Lithos* 155, 310–325. <https://doi.org/10.1016/j.lithos.2012.09.009>
- 1354 Mana, S., Furman, T., Turrin, B.D., Feigenson, M.D., Swisher, C.C., 2015. Magmatic activity
1355 across the East African North Tanzanian Divergence Zone. *J. Geol. Soc. London.* 172, 368–
1356 389. <https://doi.org/10.1144/jgs2014-072>
- 1357 Manega, P.C., 1993. Geochronology, geochemistry and isotopic study of the Plio-Pleistocene
1358 hominid sites and the Ngorongoro volcanic highland in northern Tanzania. University of
1359 Colorado at Boulder.
- 1360 Mattsson, H.B., Nandedkar, R.H., Ulmer, P., 2013. Petrogenesis of the melilititic and
1361 nephelinitic rock suites in the Lake Natron-Engaruka monogenetic volcanic field,
1362 northern Tanzania. *Lithos* 179, 175–192. <https://doi.org/10.1016/j.lithos.2013.07.012>
- 1363 Mavko, G., Mukerji, T., Dvorkin, J., 2020. *The Rock Physics Hand book*. Cambridge University
1364 Press.
- 1365 Mechie, J., Keller, G.R., Prodehl, C., Khan, M.A., Gaciri, S.J., 1997. A model for the structure,
1366 composition and evolution of the Kenya rift. *Tectonophysics* 278, 95–119.
1367 [https://doi.org/10.1016/S0040-1951\(97\)00097-8](https://doi.org/10.1016/S0040-1951(97)00097-8)
- 1368 Mollel, G.F., 2007. Petrochemistry and geochronology of Ngorongoro volcanic highland
1369 complex (NVHC) and its relationship to Laetoli and Olduvai Gorge, Tanzania. Rutgers The
1370 State University of New Jersey, School of Graduate Studies.
- 1371 Mollel, G.F., Swisher, C.C., Feigenson, M.D., Carr, M.J., 2011. Petrology, geochemistry and age
1372 of satiman, lemagurut and oldeani: Sources of the volcanic deposits of the laetoli area,
1373 in: *Vertebrate Paleobiology and Paleoanthropology*. pp. 99–119.
1374 https://doi.org/10.1007/978-90-481-9956-3_5
- 1375 Mollel, G.F., Swisher, C.C., Feigenson, M.D., Carr, M.J., 2008. Geochemical evolution of
1376 Ngorongoro Caldera, Northern Tanzania: Implications for crust-magma interaction. *Earth
1377 Planet. Sci. Lett.* 271, 337–347. <https://doi.org/10.1016/j.epsl.2008.04.014>
- 1378 Mollel, G.F., Swisher, C.C., McHenry, L.J., Feigenson, M.D., Carr, M.J., 2009. Petrogenesis of
1379 basalt-trachyte lavas from Olmoti Crater, Tanzania. *J. African Earth Sci.* 54, 127–143.
1380 <https://doi.org/10.1016/j.jafrearsci.2009.03.008>

- 1381 Moussallam, Y., Morizet, Y., Massuyeau, M., Laumonier, M., Gaillard, F., 2015. CO₂ solubility
1382 in kimberlite melts. *Chem. Geol.* 418, 198–205.
1383 <https://doi.org/10.1016/j.chemgeo.2014.11.017>
- 1384 Muirhead, J.D., Fischer, T.P., Oliva, S.J., Laizer, A., van Wijk, J., Currie, C.A., Lee, H., Judd, E.J.,
1385 Kazimoto, E., Sano, Y., Takahata, N., Tiberi, C., Foley, S.F., Dufek, J., Reiss, M.C., Ebinger,
1386 C.J., 2020. Displaced cratonic mantle concentrates deep carbon during continental
1387 rifting. *Nature* 582, 67–72. <https://doi.org/10.1038/s41586-020-2328-3>
- 1388 Mulibo, G.D., Nyblade, A.A., 2013a. Mantle transition zone thinning beneath eastern Africa:
1389 Evidence for a whole-mantle superplume structure. *Geophys. Res. Lett.* 40, 3562–3566.
1390 <https://doi.org/10.1002/grl.50694>
- 1391 Mulibo, G.D., Nyblade, A.A., 2013b. The P and S wave velocity structure of the mantle beneath
1392 eastern Africa and the African superplume anomaly. *Geochemistry, Geophys.*
1393 *Geosystems* 14, 2696–2715. <https://doi.org/10.1002/ggge.20150>
- 1394 Nakajima, J., Matsuzawa, T., Hasegawa, A., Zhao, D., 2001. Three-dimensional structure of V_p,
1395 V_s, and V_p/V_s and beneath northeastern Japan: Implications for arc magmatism and
1396 fluids. *J. Geophys. Res.* 106, 21843–21857.
- 1397 Nonnotte, P., 2007. Etude volcano-tectonique de la zone de Divergence Nord Tanzanienne
1398 (Terminaison Sud du Rift Kenyan). Caractérisation pétrologique et géochimique du
1399 volcanisme récent (8 Ma–Actuel) et du manteau source. Contraintes de mise en place.
1400 Université de Bretagne occidentale-Brest.
- 1401 Nyblade, A.A., Owens, T.J., Gurrola, H., Ritsema, J., Langston, C.A., 2000. Seismic evidence for
1402 a deep upper mantle thermal anomaly beneath East Africa. *Geology* 28, 599–602.
1403 [https://doi.org/10.1130/0091-7613\(2000\)28<599:SEFADU>2.0.CO;2](https://doi.org/10.1130/0091-7613(2000)28<599:SEFADU>2.0.CO;2)
- 1404 O'Donnell, J.P., Adams, A., Nyblade, A.A., Mulibo, G.D., Tugume, F., 2013. The uppermost
1405 mantle shear wave velocity structure of eastern africa from rayleigh wave tomography:
1406 Constraints on rift evolution. *Geophys. J. Int.* 194, 961–978.
1407 <https://doi.org/10.1093/gji/ggt135>
- 1408 O'Reilly, S.Y., Griffin, W.L., 2013. Mantle metasomatism, Lecture Notes in Earth System
1409 Sciences. https://doi.org/10.1007/978-3-642-28394-9_12
- 1410 O'Reilly, S.Y., Griffin, W.L., 1988. Mantle metasomatism beneath western Victoria, Australia:
1411 I. Metasomatic processes in Cr-diopside Iherzolites. *Geochim. Cosmochim. Acta* 52, 433–
1412 447.
- 1413 Passchier, C.W., Trouw, R.A.J., 2005. *Microtectonics*. Springer Science and Business Media.
- 1414 Peng, Y., Mookherjee, M., 2020. Thermoelasticity of tremolite amphibole: Geophysical
1415 implications. *Am. Mineral.* 105, 904–916. <https://doi.org/10.2138/am-2020-7189>
- 1416 Pik, R., Marty, B., Hilton, D.R., 2006. How many mantle plumes in Africa? The geochemical
1417 point of view. *Chem. Geol.* 226, 100–114.

- 1418 <https://doi.org/10.1016/j.chemgeo.2005.09.016>
- 1419 Plasman, M., Tiberi, C., Ebinger, C., Gautier, S., Albaric, J., Peyrat, S., Déverchère, J., Le Gall, B.,
1420 Tarits, P., Roecker, S., Wambura, F., Muzuka, A., Mulibo, G., Mtelela, K., Msabi, M., Kianji,
1421 G., Hautot, S., Perrot, J., Gama, R., 2017. Lithospheric low-velocity zones associated with
1422 a magmatic segment of the Tanzanian Rift, East Africa. *Geophys. J. Int.* 210, 465–481.
1423 <https://doi.org/10.1093/gji/ggx177>
- 1424 Priestley, K., Mckenzie, D., Debayle, E., Pilidou, S., 2008. The African upper mantle and its
1425 relationship to tectonics and surface geology. *Geophys. J. Int.* 175, 1108–1126.
1426 <https://doi.org/10.1111/j.1365-246X.2008.03951.x>
- 1427 Putirka, K.D., 2008. Thermometers and barometers for volcanic systems. *Rev. Mineral.*
1428 *Geochemistry* 69, 61–120. <https://doi.org/10.2138/rmg.2008.69.3>
- 1429 Reichmann, H.J., Jacobsen, S.D., 2004. High-pressure elasticity of a natural magnetite crystal.
1430 *Am. Mineral.* 89, 1061–1066. [https://doi.org/https://doi-](https://doi.org/https://doi-org.insu.bib.cnrs.fr/10.2138/am-2004-0718)
1431 [org.insu.bib.cnrs.fr/10.2138/am-2004-0718](https://doi.org/https://doi-org.insu.bib.cnrs.fr/10.2138/am-2004-0718)
- 1432 Reiss, M.C., Muirhead, J.D., Laizer, A.S., Link, F., Kazimoto, E.O., Ebinger, C.J., Rumpker, G.,
1433 2021. The Impact of Complex Volcanic Plumbing on the Nature of Seismicity in the
1434 Developing Magmatic Natron Rift, Tanzania. *Front. Earth Sci.* 8, 1–21.
1435 <https://doi.org/10.3389/feart.2020.609805>
- 1436 Roberts, M.A., 2003. *Geochemical and Volcanological Evolution of the Mt. Meru Region,*
1437 *northern Tanzania.* University of Cambridge.
- 1438 Rudnick, R.L., McDonough, W.F., Orpin, A., 1994. Northern Tanzanian peridotite xenoliths: a
1439 comparison with Kaapvaal peridotites and inferences on metasomatic interactions.
1440 (Meyer, H.O.A. Leonards, O., eds.) *Kimberlites, Relat. Rocks Mantle Xenoliths, Proc. 5th*
1441 *Int. Kimberl. Conf. C.P.R.M, Bras.* 1, 336–353.
- 1442 Sakamaki, T., Ohtani, E., Urakawa, S., Suzuki, A., Katayama, Y., 2010. Density of dry peridotite
1443 magma at high pressure using an X-ray absorption method. *Am. Mineral.* 95, 144–147.
1444 <https://doi.org/10.2138/am.2010.3143>
- 1445 Sakamaki, T., Ohtani, E., Urakawa, S., Suzuki, A., Katayama, Y., 2009. Measurement of hydrous
1446 peridotite magma density at high pressure using the X-ray absorption method. *Earth*
1447 *Planet. Sci. Lett.* 287, 293–297. <https://doi.org/10.1016/j.epsl.2009.07.030>
- 1448 Sakamaki, T., Ohtani, E., Urakawa, S., Terasaki, H., Katayama, Y., 2011. Density of carbonated
1449 peridotite magma at high pressure using an X-ray absorption method. *Am. Mineral.* 96,
1450 553–557. <https://doi.org/10.2138/am.2011.3577>
- 1451 Sang, L., Bass, J.D., 2014. Single-crystal elasticity of diopside to 14GPa by Brillouin scattering.
1452 *Phys. Earth Planet. Inter.* 228, 75–79. <https://doi.org/10.1016/j.pepi.2013.12.011>
- 1453 Selway, K., Yi, J., Karato, S.I., 2014. Water content of the Tanzanian lithosphere from
1454 magnetotelluric data: Implications for cratonic growth and stability. *Earth Planet. Sci.*

- 1455 Lett. 388, 175–186. <https://doi.org/10.1016/j.epsl.2013.11.024>
- 1456 Sherrod, D.R., Magigita, M.M., Kwelwa, S., 2013. Geologic Map of Oldonyo Lengai (Oldoinyo
1457 Lengai) volcano and surroundings, Arusha Region, United Republic of Tanzania. USGS
1458 Open-File Rep.
- 1459 Smith, M., Mosley, P., 1993. Crustal heterogeneity and basement influence on the
1460 development of the Kenya rift, East Africa. *Tectonics* 12, 591–606.
- 1461 Sobolev, S. V., Zeyen, H., Stoll, G., Werling, F., Altherr, R., Fuchs, K., 1996. Upper mantle
1462 temperatures from teleseismic tomography of French Massif Central including effects of
1463 composition, mineral reactions, anharmonicity, anelasticity and partial melt. *Earth
1464 Planet. Sci. Lett.* 139, 147–163. [https://doi.org/10.1016/0012-821x\(95\)00238-8](https://doi.org/10.1016/0012-821x(95)00238-8)
- 1465 Soltanmohammadi, A., Grégoire, M., Rabinowicz, M., Gerbault, M., Ceuleneer, G., Rahgoshay,
1466 M., Bystricky, M., Benoit, M., 2018. Transport of volatile-rich melt from the mantle
1467 transition zone via compaction pockets: Implications for mantle metasomatism and the
1468 origin of Alkaline Lavas in the Turkish-Iranian plateau. *J. Petrol.* 59, 2273–2310.
1469 <https://doi.org/10.1093/petrology/egy097>
- 1470 Stixrude, L., Lithgow-Bertelloni, C., 2005. Mineralogy and elasticity of the oceanic upper
1471 mantle: Origin of the low-velocity zone. *J. Geophys. Res. Solid Earth* 110, 1–16.
1472 <https://doi.org/10.1029/2004JB002965>
- 1473 Tiberi, C., Gautier, S., Ebinger, C., Roecker, S., Plasman, M., Albaric, J., Peyrat, S., Perrot, J.,
1474 Wambura, R.F., Msabi, M., Muzuka, A., Mulibo, G., Kianji, G., 2019. Lithospheric
1475 modification by extension and magmatism at the craton-orogenic boundary: North
1476 Tanzania Divergence, East Africa. *Geophys. J. Int.* 216, 1693–1710.
1477 <https://doi.org/10.1093/gji/ggy521>
- 1478 Tommasi, A., Godard, M., Coromina, G., Dautria, J.M., Barszczus, H., 2004. Seismic anisotropy
1479 and compositionally induced velocity anomalies in the lithosphere above mantle plumes:
1480 A petrological and microstructural study of mantle xenoliths from French Polynesia. *Earth
1481 Planet. Sci. Lett.* 227, 539–556. <https://doi.org/10.1016/j.epsl.2004.09.019>
- 1482 Tommasi, A., Tikoff, B., Vauchez, A., 1999. Upper mantle tectonics: Three-dimensional
1483 deformation, olivine crystallographic fabrics and seismic properties. *Earth Planet. Sci.
1484 Lett.* 168, 173–186. [https://doi.org/10.1016/S0012-821X\(99\)00046-1](https://doi.org/10.1016/S0012-821X(99)00046-1)
- 1485 Vauchez, A., Dineur, F., Rudnick, R., 2005. Microstructure, texture and seismic anisotropy of
1486 the lithospheric mantle above a mantle plume: Insights from the Labait volcano xenoliths
1487 (Tanzania). *Earth Planet. Sci. Lett.* 232, 295–314.
1488 <https://doi.org/10.1016/j.epsl.2005.01.024>
- 1489 Watanabe, T., 1993. Effects of water and melt on seismic velocities and their application to
1490 characterization of seismic reflectors. *Geophys. Res. Lett.* 20, 2933–2936.
1491 <https://doi.org/10.1029/93GL03170>
- 1492 Weeraratne, D.S., Forsyth, D.W., Fischer, K.M., Nyblade, A.A., 2003. Evidence for an upper

1493 mantle plume beneath the Tanzanian craton from Rayleigh wave tomography. J.
1494 Geophys. Res. Solid Earth 108. <https://doi.org/10.1029/2002jb002273>

1495 Wilkinson, P., Mitchell, J.G., Cattermole, P.J., Downie, C., 1986. Volcanic chronology of the
1496 Meru-Kilimanjaro region, northern Tanzania. J. Geol. Soc. London. 143, 601–605.
1497 <https://doi.org/10.1144/gsjgs.143.4.0601>

1498 Wölbern, I., Rümpker, G., Link, K., Sodoudi, F., 2012. Melt infiltration of the lower lithosphere
1499 beneath the Tanzania craton and the Albertine rift inferred from S receiver functions.
1500 Geochemistry, Geophys. Geosystems 13, 1–20. <https://doi.org/10.1029/2012GC004167>

1501 Ziberna, L., Klemme, S., Nimis, P., 2013. Garnet and spinel in fertile and depleted mantle:
1502 Insights from thermodynamic modelling. Contrib. to Mineral. Petrol. 166, 411–421.
1503 <https://doi.org/10.1007/s00410-013-0882-5>

1504

1505

1506

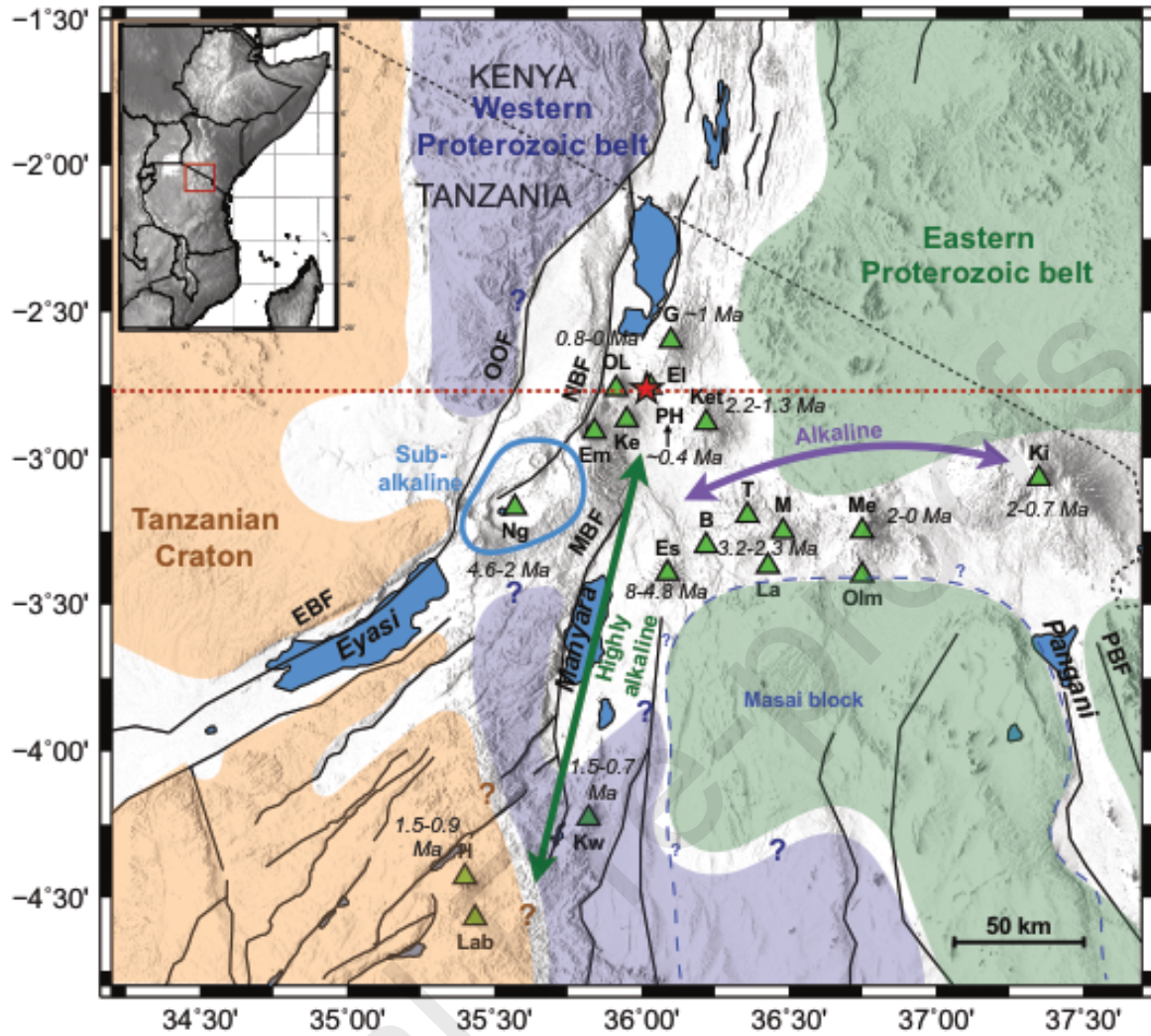
1507 **3 Highlights (<85 characters):**

- 1508 - Mantle at rift initiation is metasomatized by alkaline fluids at 40-90 km depth
- 1509 - 1100°C mantle isotherm relates to the volatile-bearing peridotite solidus
- 1510 - Lithospheric mantle has ≈20% of crystallized or ≈10% of fluid-filled vertical veins

1511

Figure1

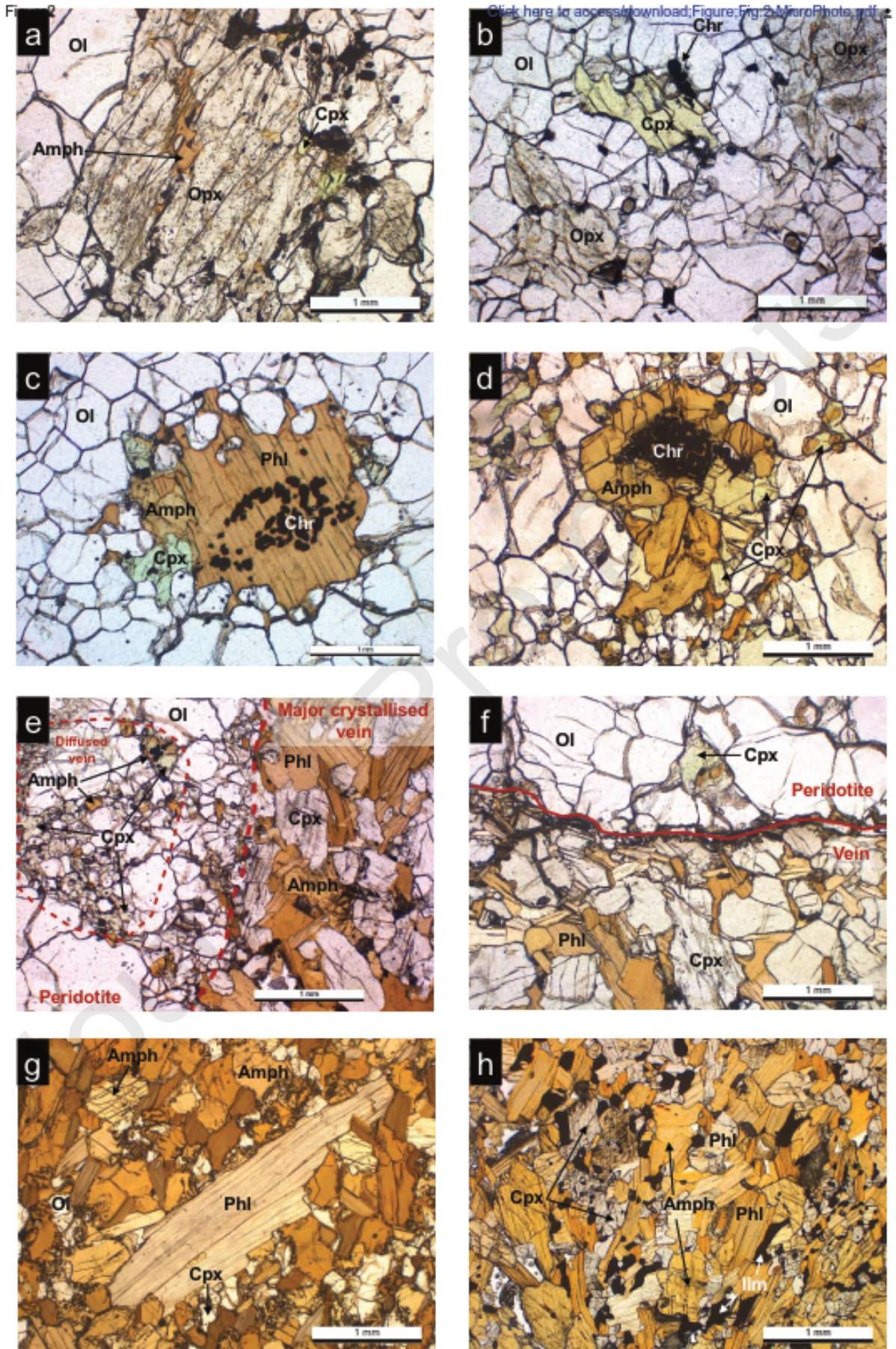
[Click here to access/download;Figure;Fig.1-Geol.pdf](#)



1512

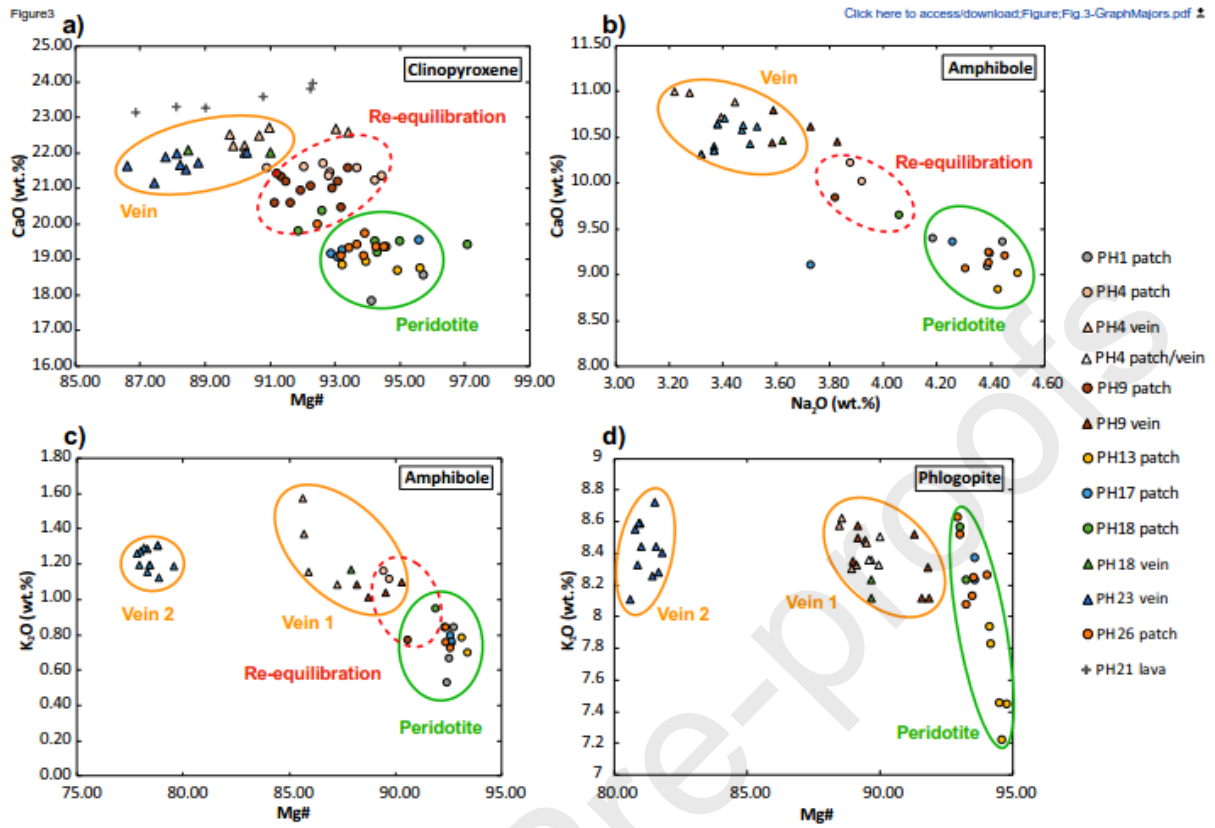
1513

1514



1515

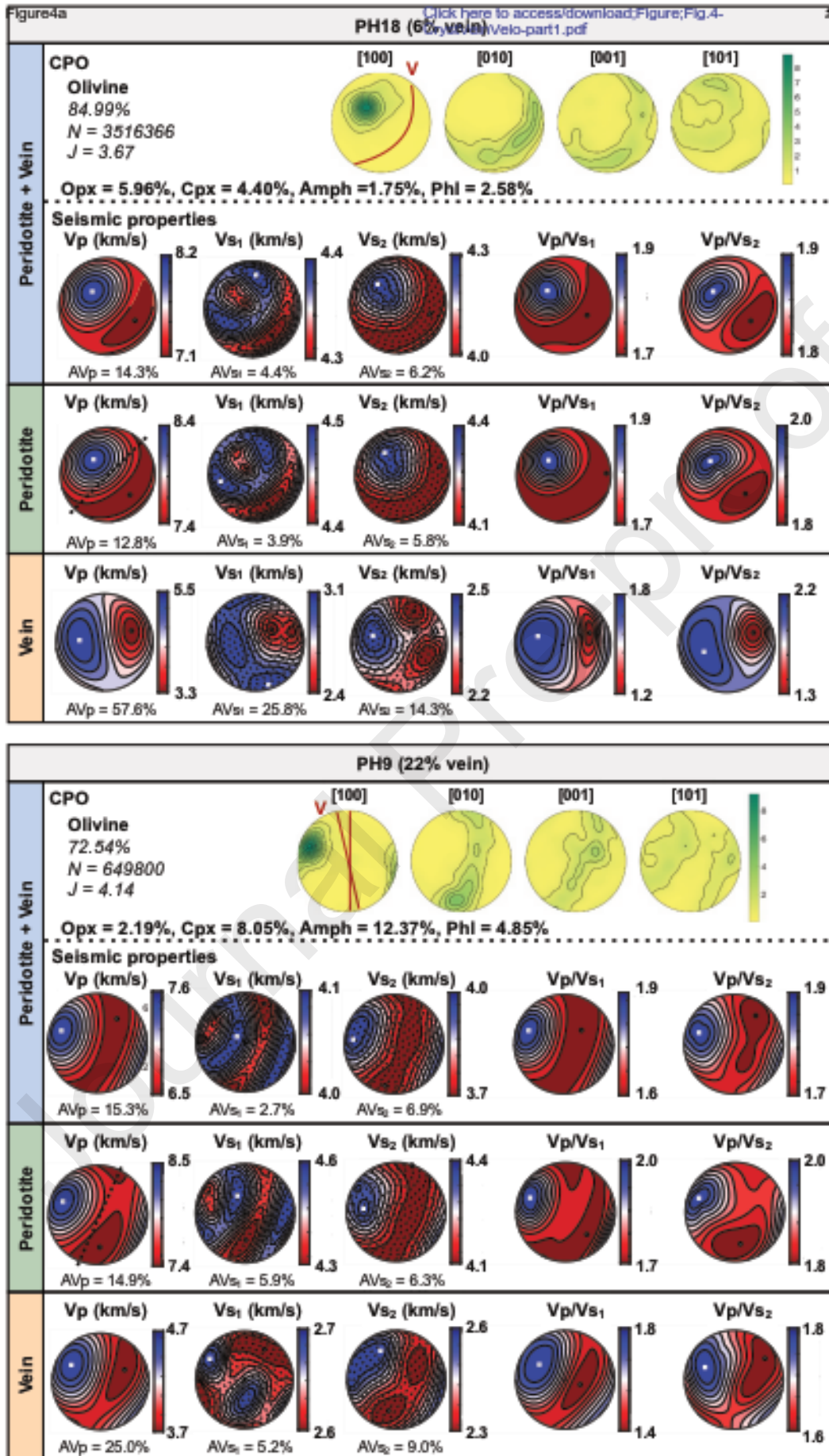
1516



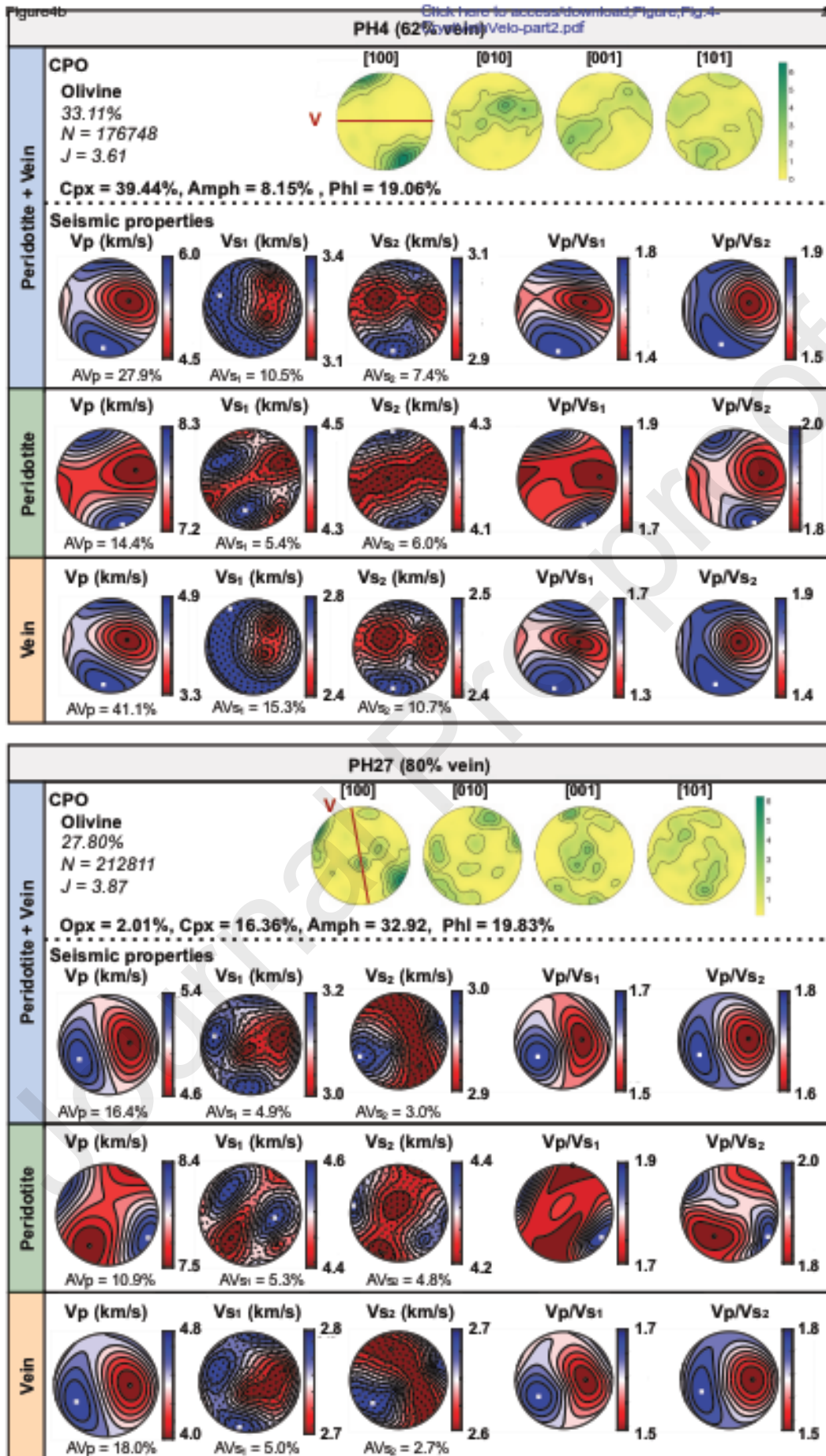
1517

1518

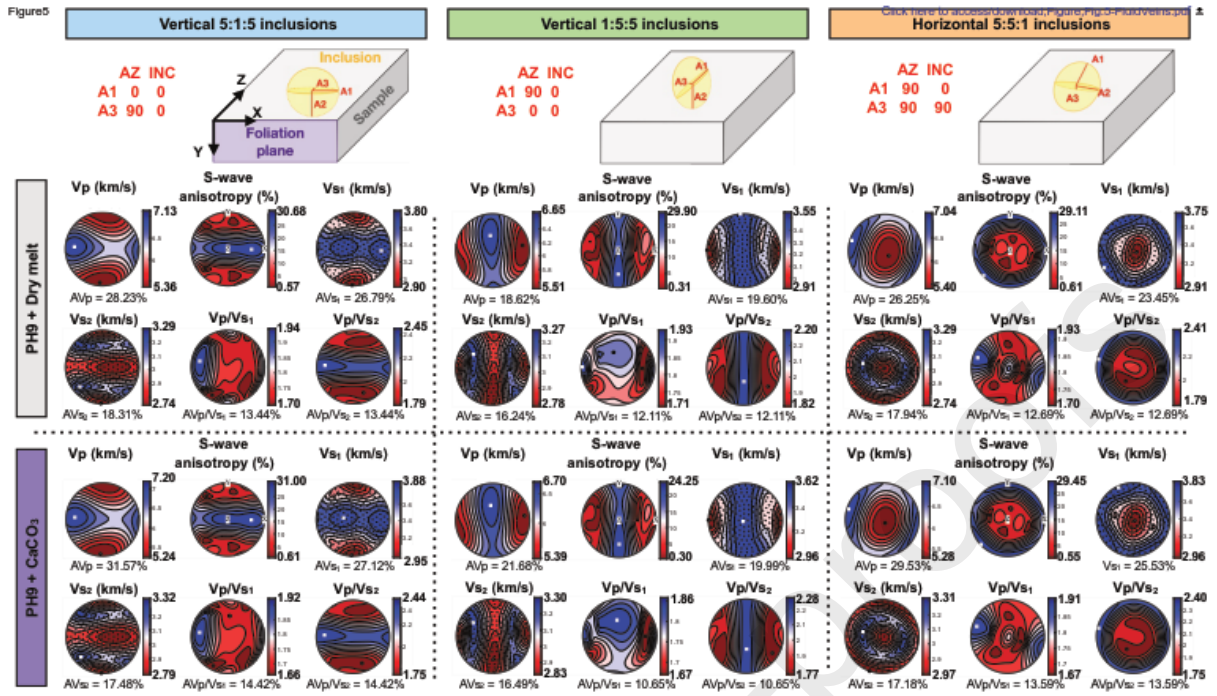
1519



Journal Pre-proofs



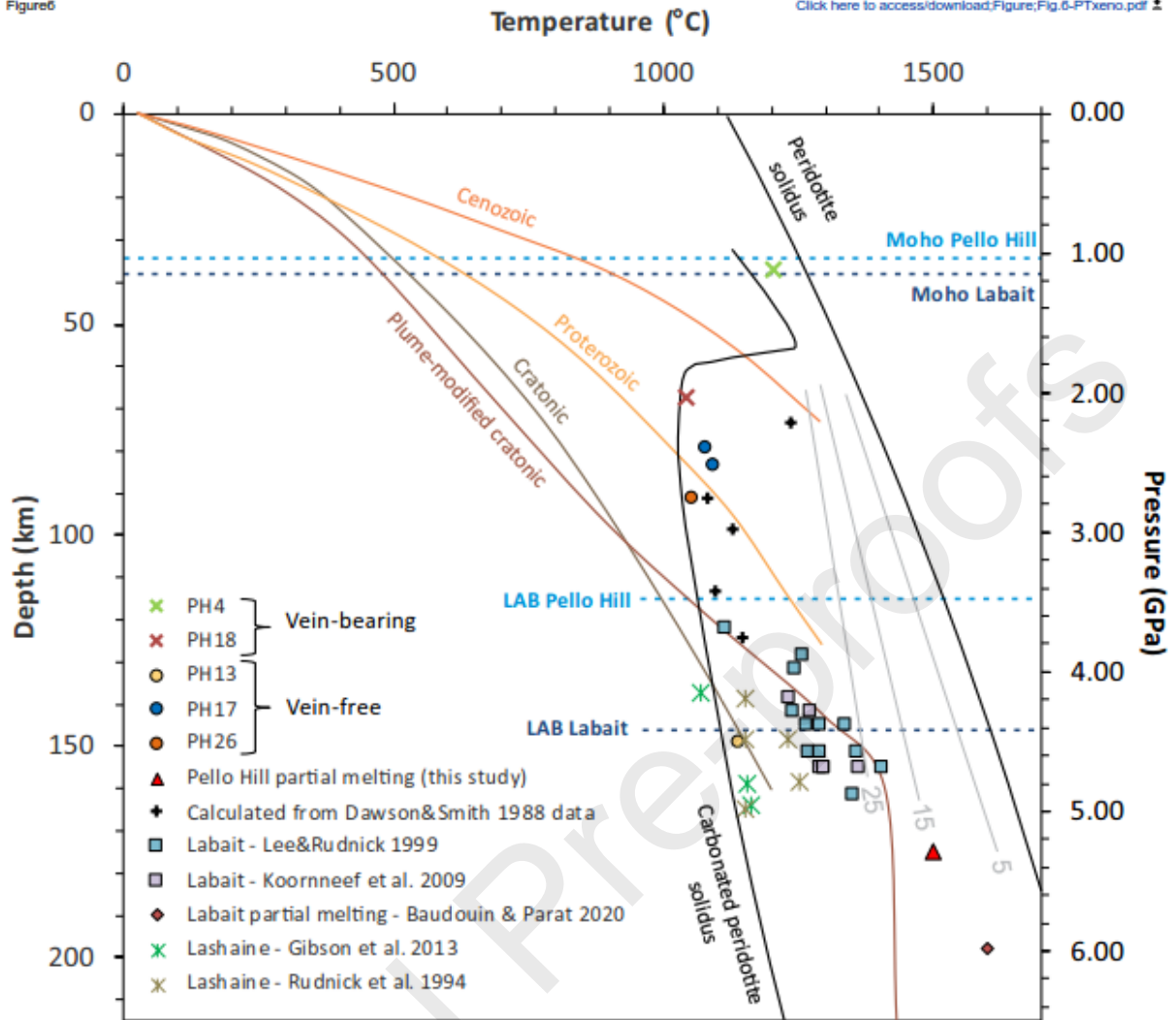
1523



1524

1525

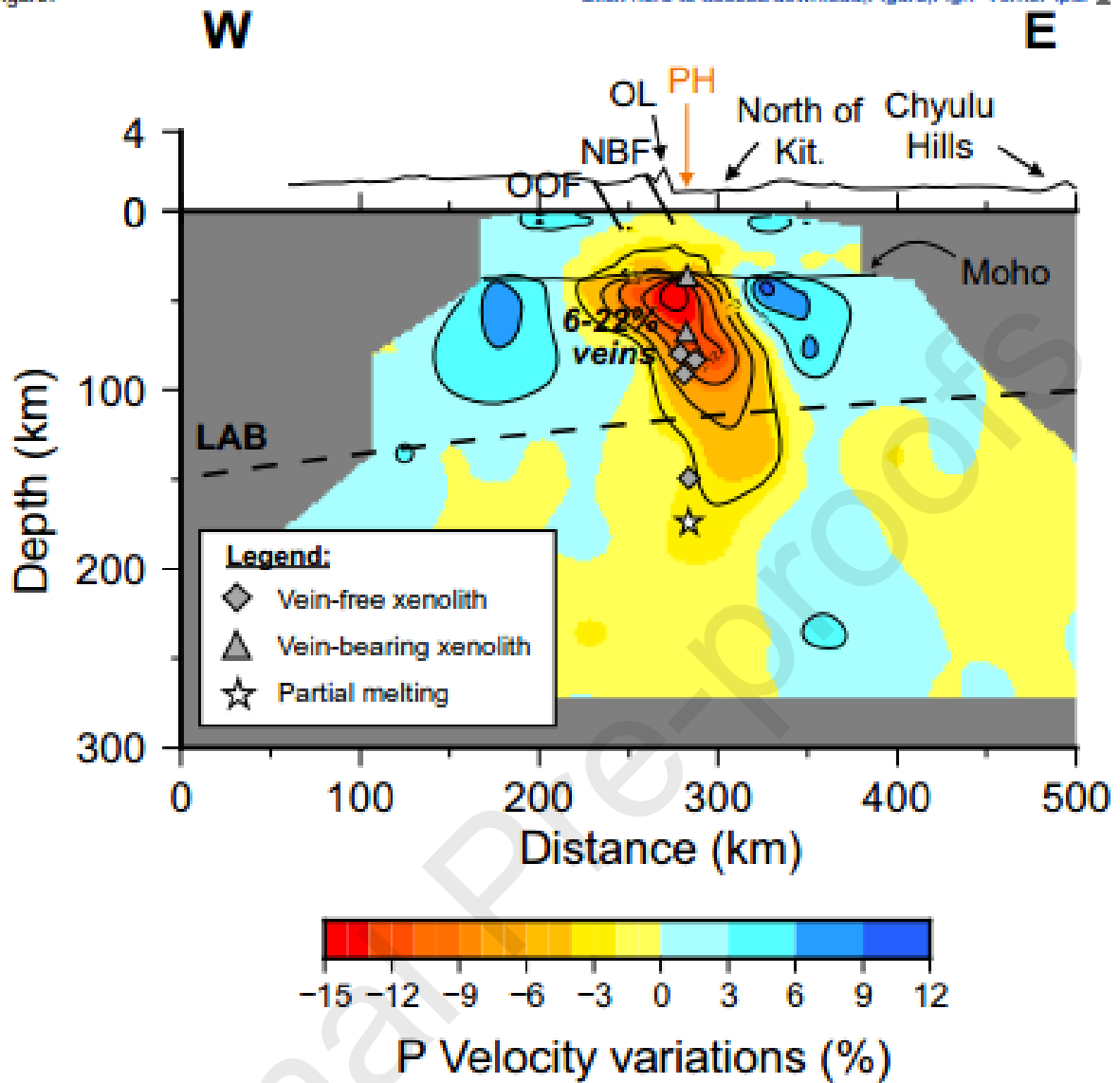
Figure 6

[Click here to access/download;Figure;Fig.6-PTxeno.pdf](#)

1526

1527

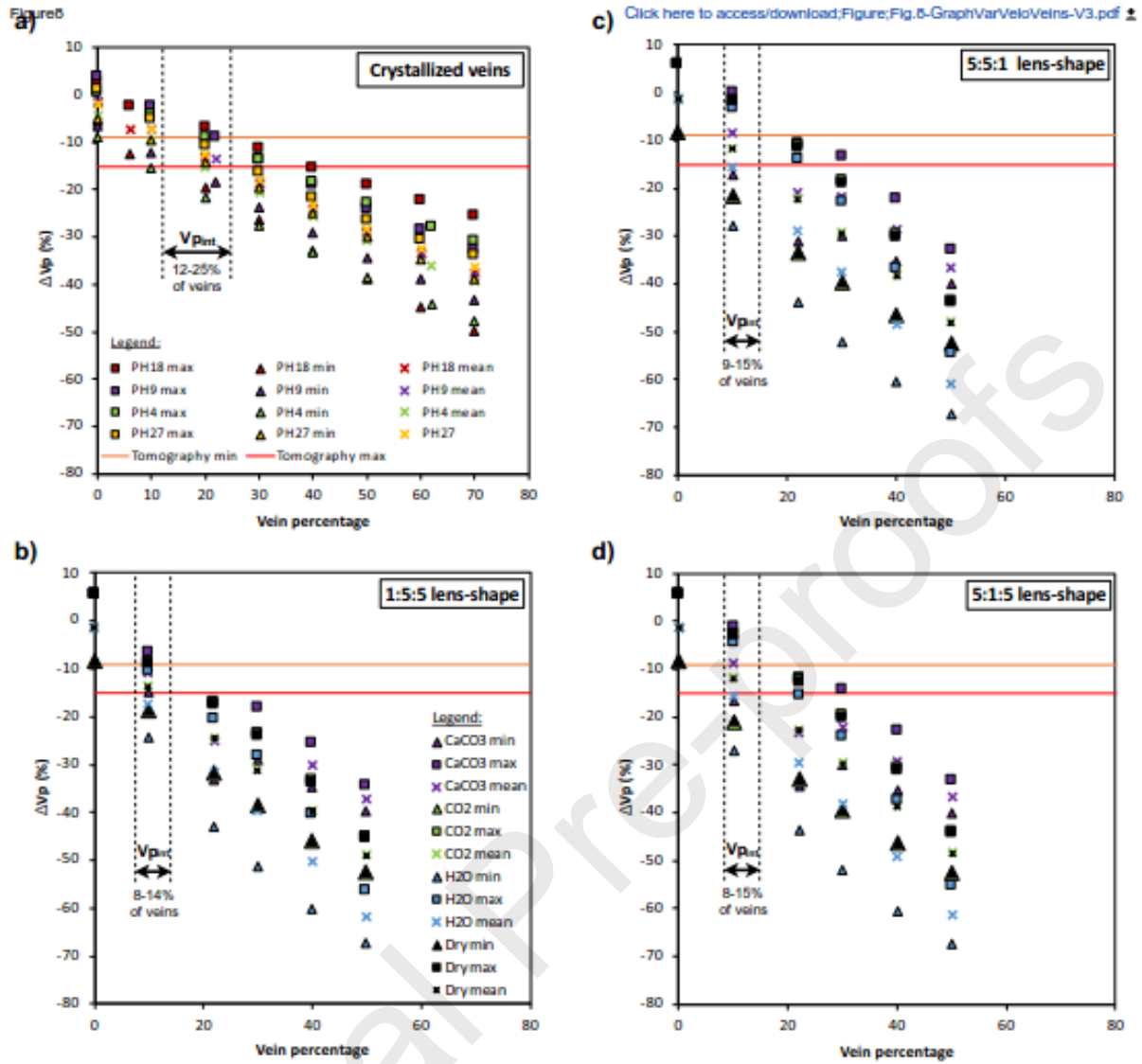
Figure 7

[Click here to access/download;Figure;Fig.7-TomoP.pdf](#)

1528

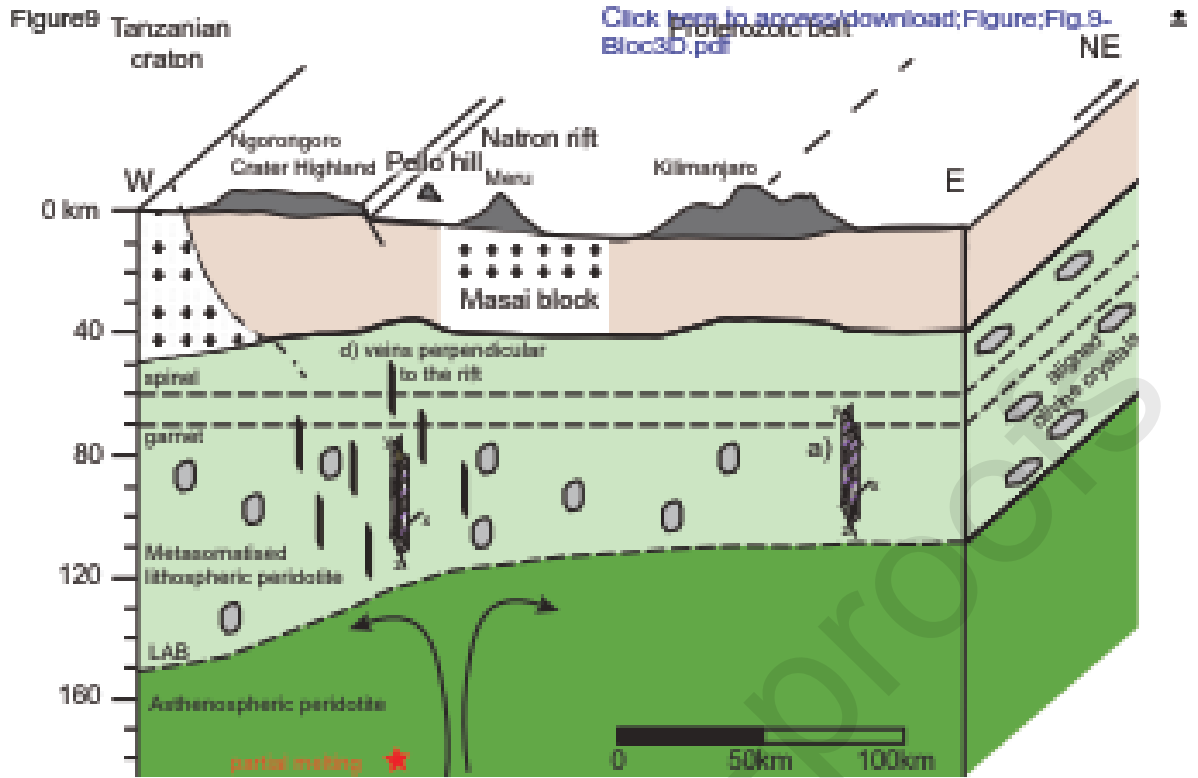
1529

Figure 8

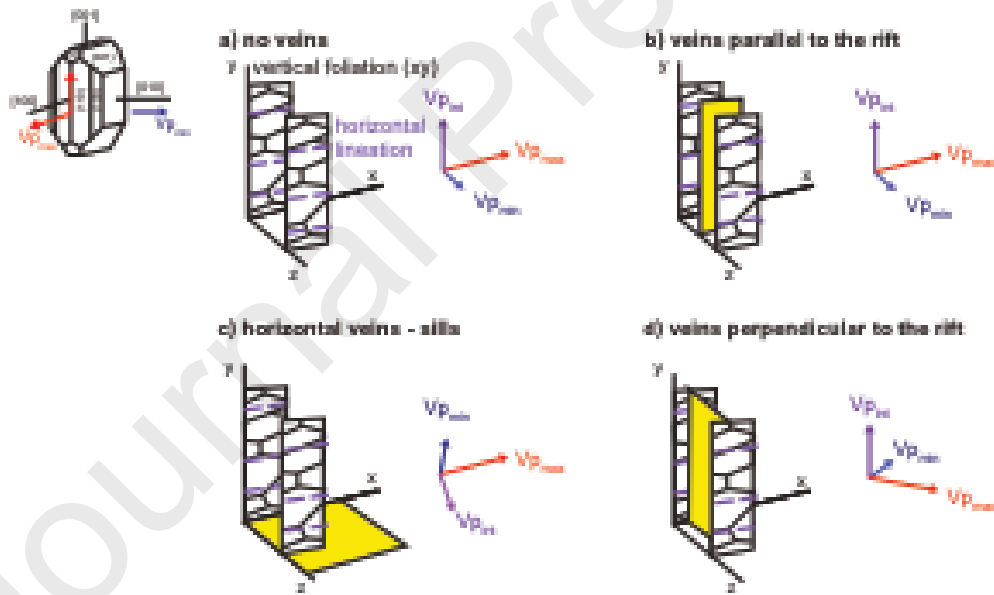


1530

1531



Vertical foliation (xy) and horizontal lineation in peridotite



1532